Available online at www.sciencedirect.com
ScienceDirect
Trans. Nonferrous Met. Soc. China 32(2022) 377−410
Transactions of Nonferrous Metals Society of China
www.tnmsc.cn

Corrosion resistances of metallic materials in environments containing chloride ions: A review

Xian-man ZHANG[1], Zai-yu CHEN[1], Hong-feng LUO[1], Teng ZHOU[1], Yu-liang ZHAO[2], Zi-cheng LING[3]

1. Mechanical and Electrical Engineering College, Hainan University, Haikou 570228, China;
2. Neutron Scattering Technical Engineering Research Centre, School of Mechanical Engineering, Dongguan University of Technology, Dongguan 523808, China;
3. School of Materials Science and Engineering, North China University of Water Resources and Electric Power, Zhengzhou 450045, China

Received 18 January 2021; accepted 2 September 2021

Abstract: Corrosion, more specifically, pitting corrosion happening extremely in marine environments, leads to lifespan of materials drastically decreasing in service, which causes enormous economic loss and even environmental disaster and casualties. In the past decade, increasing efforts have been made to study the corrosion behaviors of materials in chloride-containing aqueous environments. Herein, this work provides an overview of recent progress in understanding the degradation mechanism and improving the corrosion resistance and corrosion-wear resistance of materials from bulk metal to surface treatment involving organic coating, metal and its alloy or compound coating. The particular emphasis is given to the periodic layered structures (PLSs), whose anti-corrosion properties outperformed others to some extent, wherever in terms of bulk metal or surface treatment, regardless of aggressive environment (corrosion or corrosion-wear conditions). Numerical simulation based on kinds of models at different scales is introduced to deeply understand the process of corrosion and/or corrosion-wear in chloride-containing aqueous environment. Combined experimental result with numerical simulation, the micro-galvanic corrosion dominated degradation mechanism of PLSs is critically analyzed. Types of setups to realize corrosion-wear in laboratory are also summarized. At last, future research and development are prospected, offering to develop a basic application of PLSs designed by corrosion protection methodology in the near future.

Key words: pitting corrosion; chloride ion; periodic layered structure; galvanic corrosion; degradation mechanism

1 Introduction

1.1 Corrosion and its adverse effect

The deterioration of mechanical properties caused by a chemical or electrochemical reaction between material and its environment is called corrosion [1], which is an old issue in the field of material science and engineering. Corrosion is a kind of spontaneous and quiet destruction, but its harm is very serious, as shown in Fig. 1 [2]. The forms of corrosion are various. Compared with the corrosion caused by high temperature molten metal under extreme conditions which was reviewed by ZHANG and CHEN [3], the corrosion caused by electrochemical reaction occurs commonly in our daily life. Therefore, it is critical to summarize the corrosion caused by electrochemical reaction. During the electrochemical corrosion process, the metal changed back to its metal compound and lost the original metal characteristics, resulting in the impairment of the performance and durability of materials. The dissolution of metal (M) during the anodic reaction is based on the following formula:

Corresponding author: Xian-man ZHANG, Tel: +86-898-66267372, E-mail: xianman213@163.com
DOI: 10.1016/S1003-6326(22)65802-3

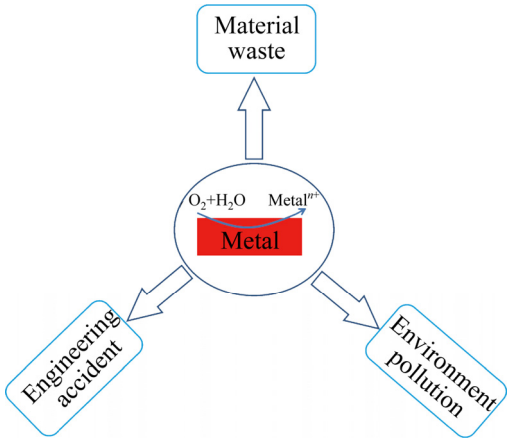

Fig. 1 Harms of metal electrochemical corrosion [2]

$$M \rightarrow M^{n+} + ne \quad (1)$$

Enormous economic losses and even environmental disaster and casualties are caused by corrosion of materials every year in the world. It was internationally recognized that the loss caused by corrosion in every country was as high as 3%–5% of the gross domestic product (GDP) [4]. In 2016, the American Society of Corrosion Engineers announced the latest corrosion survey results: the global corrosion cost was estimated to be US$2.5 trillion [5,6]. In China, in 2015, the Chinese Academy of Engineering launched a major consulting project of "Research on Chinese corrosion status and control strategy". The results showed that in 2014, China's annual corrosion cost accounted for about 3.34% of GDP [1,7].

The ocean is rich in resources, and has great potential economic interests and strategic national defense status. However, the problem of marine corrosion (see Fig. 2 [8]) is one of the main threats in the process of ocean exploitation. Marine corrosion loss accounts for about 30% of the total corrosion loss. Marine platforms such as ships, cross sea bridges and offshore structures immersed in seawater for a long time suffer from seawater corrosion, especially when they have been in service for more than 15−20 years, the risk of accidents caused by seawater corrosion increases dramatically [9]. Catastrophic incidents, such as the Castor failure in USA in 2000 [10] and the "11·22" explosion in Qingdao of China in 2013, had highlighted the on-going corrosion issues [11]. Therefore, the investigation of corrosion behavior and design of high corrosion-resistant materials in marine environment are urgently needed.

Fig. 2 Corrosion of ship propeller caused by seawater [8]

1.2 Driving force of electrochemical corrosion

Human experience has shown that all spontaneous processes are directional. From the thermodynamics point of view, electrochemical corrosion is an inherent property of metal and their alloys due to their natural tendency for oxidation to reduce the Gibbs free energy. Generally, a negative changed value of standard Gibbs free energy (ΔG^0) means the possibility of corrosion reaction. The more negative the value of ΔG^0, the more the instability of metals, subsequently the higher the corrosion tendency. The basic reason for the spontaneous reaction of electrochemical corrosion lies on the existence of depolarizing agent (i.e., NaCl solution) in the surrounding environment to oxidize a metal into a metal cation or its compound. Indeed, the ΔG^0 is only thought to be associated with high electrochemical corrosion tendency [12]. The corrosion rate belongs to dynamic category, which can be influenced by kinds of factors during the electrochemical reaction. The influencing factors mainly included: (1) the metallic material itself including the composition and crystal structure of metal, inhomogeneity in the metal, heat-treatment history, surface condition (i.e., crack, cavity or inclusion), surface roughness, deformation and stress, and (2) the surrounding environment factors such as oxygen and its concentration, chloride adsorption and incorporation into the passive film, humidity, temperature, pH, pressure, biomass and the flow rate of the solution [12,13]. It is also related to the rationality of equipment design, manufacture and maintenance procedures.

1.3 Insight into mechanism of ionic chloride corrosion

Seawater is an aggressive corrosive

environment, and marine corrosion is an extremely complex process, including marine atmospheric corrosion, seawater erosion-corrosion, chloride ion (Cl^-) corrosion, microbiologically influenced corrosion, sediment erosion-corrosion and their complex interactions. Due to the large amount of NaCl and $MgCl_2$ in seawater, the concentration of Cl^- is very high, even reaches 26 g/L [14]. The common corrosion characteristic of Cl^- corrosion is localized attack, also called pitting corrosion, which occurs at discrete areas and is a great risk issue in most engineering systems. It is evident that pitting corrosion remarkably differs from general corrosion characterised by a uniform attack of the exposed surface. General corrosion is generally a slow process. While, the penetration rate of pitting corrosion can reach 100 times that of uniform corrosion [15]. Pitting corrosion occurs when isolated sites of a material suffer from rapid attack due to the local breakdown of protective passivity, while, most of the adjacent surfaces remain virtually unaffected, as shown in Fig. 3 [16]. It is worthy of notice that the dissolution of the other inactive surface also takes place at a greatly slower rate than that of the active anodic.

The excellent corrosion resistance of stainless steel is attributed to the formation of a dense Cr_2O_3-rich passive film on nanometer scale on its surface. However, Cl^- is a kind of active anion with strong permeability and erosiveness, which enables diffusion through the defects on the passive film onto the metal substrate and enhances corrosion by initiation and propagation of pitting corrosion. Pitting corrosion is one of the most destructive types of metal loss, which is especially dangerous for the marine and offshore steel structures [16]. Cl^- induced pitting corrosion is recognized as the leading factor for the breakdown of local passive film [17], which can seriously attack the protective passive film, resulting in pitting corrosion and loose porous structure on the corroded surface. Released abundant metal cations by anode dissolution are easy to accumulate inside the pit, and attract Cl^- to react with them, causing the pH decreasing. Furthermore, the autocatalytic process of corrosion reaction is accelerated. Cl^- has a strong adsorption effect, which can hinder metal passivation; Cl^- also has electric field effect and forms soluble complexes to accelerate metal anodic dissolution, and finally leads to corrosion degradation of metal materials for marine equipment in the forms of pinhole or crack-development. The auto-catalytic mechanism of Cl^- accelerating anodic dissolution (Fig. 4 [18] and Fig. 5) of iron and steel is as follows:

$$Fe+Cl^-+H_2O \rightleftharpoons [FeCl(OH)^-]_{ads}+H^++e \quad (2)$$

$$[FeCl(OH)^-]_{ads} \rightleftharpoons FeClOH+e \quad (3)$$

$$FeClOH+H^+ \rightleftharpoons Fe^{2+}+Cl^-+H_2O \quad (4)$$

Overall, pitting corrosion is proved to be controlled by the diffusion process under a metal chloride salt layer. Three stages including passive film breakdown/pit nucleation, metastable pit growth and stable pit growth are at least contained in the pitting process. Once pitting initiates in some discrete areas (i.e., grain boundaries, inclusions and

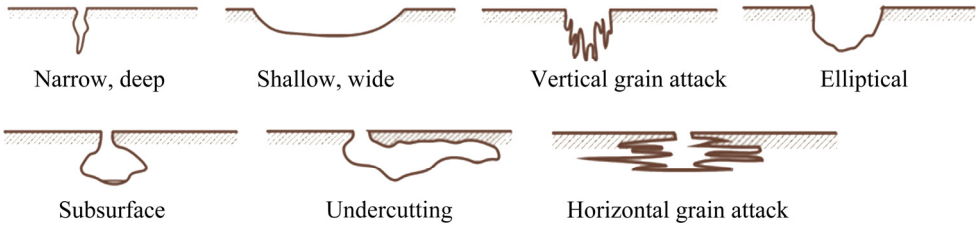

Fig. 3 Schematic diagram of realistic morphologies of pitting corrosion [16]

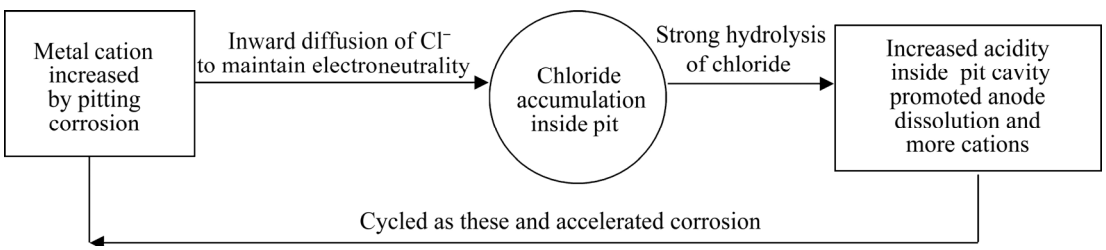

Fig. 4 Process of auto-catalytic mechanism of Cl^- [18]

other surface defects) of metal surface [19] after the induction time and reaches a critical depth [20], it propagates at a fast rate due to both effects of the acidity of the solution inside the pit that prevents the repassivation and the salt film formed on the pit surface that enhances the stability, which is characterised by the pitting potential (φ_{pit}) [21]. Consequently, perforation of metal occurs by conversation of the new pit formed by pit reactivation and the pre-existing pit (Fig. 6 [22]).

Since H^+ is also produced in this corrosion reaction, H_2 is often formed on the cathode side by Reaction (5). H_2 evolution is a most common cathodic reaction process since it is quite common to come across acidic environments when studying corrosion problems. As depicted in Fig. 7 [23,24], during corrosion processes, the amount of dissolved hydrogen in solution increases gradually until it reaches a certain critical value at which gas bubble formation removes the H_2 from solution. The evolution of H_2, which is also considered to evaluate the average corrosion rate of Mg alloy (one hydrogen molecule is evolved for every Mg atom dissolved), has a great impact on the corrosion product deposed on the surface of cathodic layer and can be collected by apparatus as shown in Fig. 8 [25]. Moreover, the presence of Cl^- in the solution stifles the repassivation tendency of a pit or crack and facilitates H evolution and H penetration [26], which causes the corroded metal

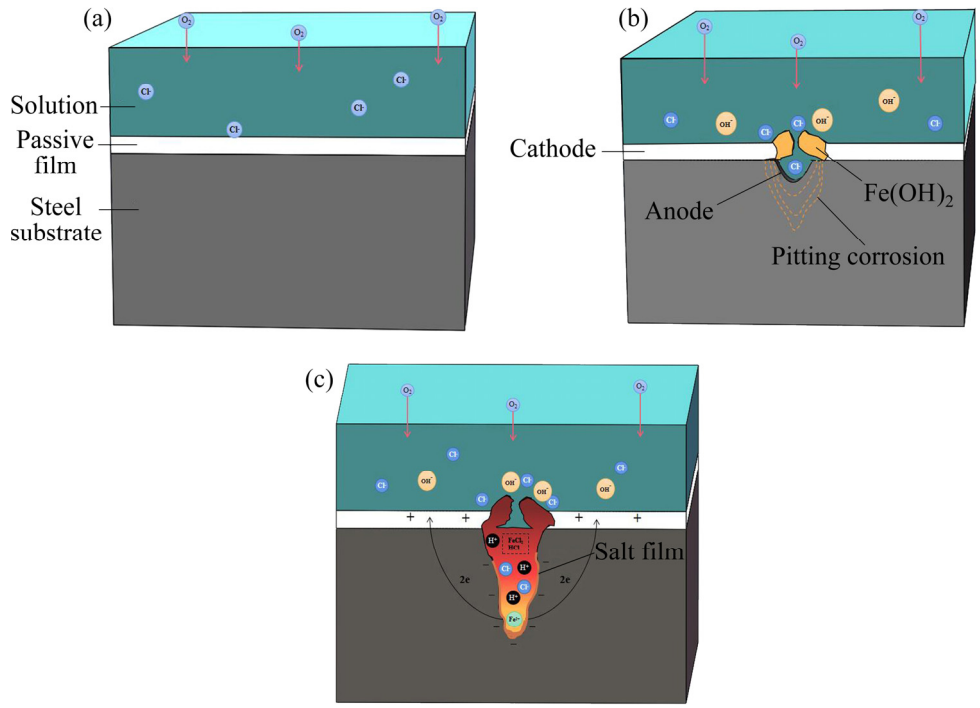

Fig. 5 Schematic illustration of pitting corrosion in Cl^--containing aqueous environments

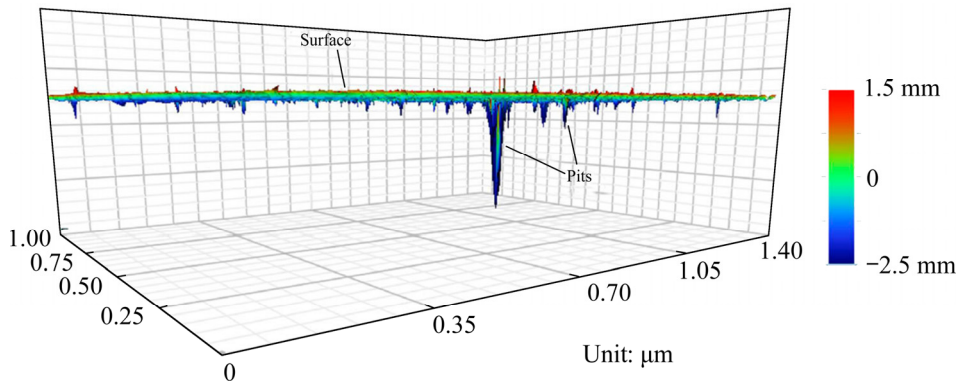

Fig. 6 Morphology profile of pits observed under 3D optical profilometer [22]

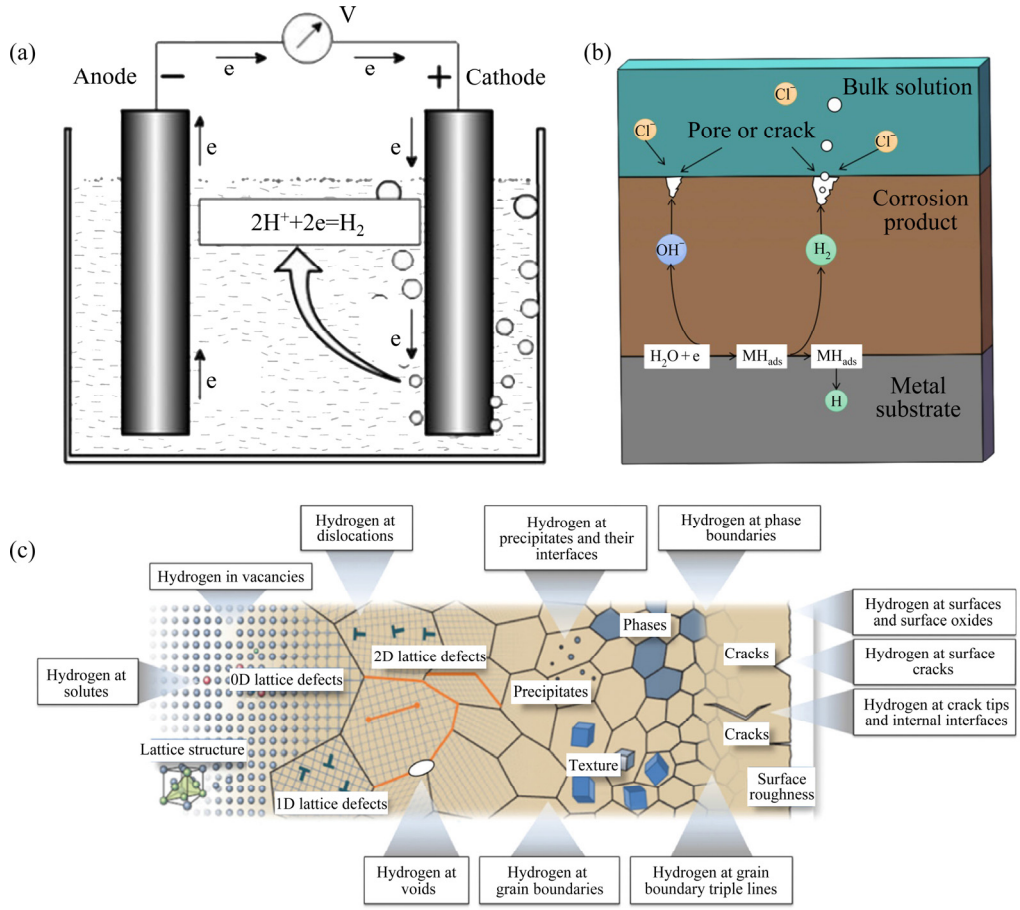

Fig. 7 Schematic diagram of reduction of hydrogen in acid electrolyte [23] (a), formation (b) and permeation (c) of hydrogen during corrosion [24] (The arrows illustrate the transportation and trapping sites)

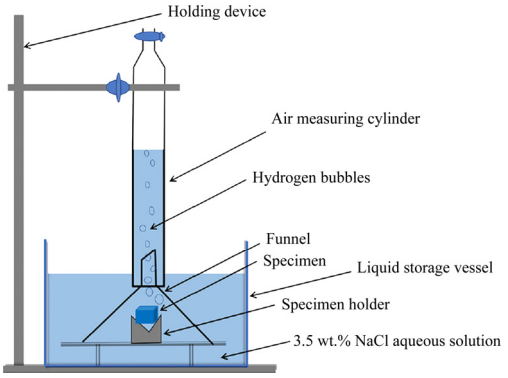

Fig. 8 Schematic illustration of apparatus used to measure volume of hydrogen evolution [25]

to be at the great risk of hydrogen embrittlement (HE) especially for the high strength steel with the strength larger than 1200 MPa [27,28]. The diffusion of H atoms plays a crucial role in H induced crack. H atoms can not only diffuse between interstitial lattice sites in H-charged metals, more importantly, but also be trapped by the imperfections like dislocations, grain boundaries, interfaces, vacancies, micro voids or any other lattice defect [29]. The diffusion driving force of H atoms is the both gradients of H concentration and H stress. Till now, H-enhanced decohesion, H-enhanced localized plasticity, H-enhanced and strain-induced vacancies, even a combination of these, have been developed to understand fully the mechanism of HE [30].

$$2H^{+}+2e\rightarrow H_2 \quad (5)$$

2 Corrosion resistance of metallic materials in Cl^{-}-containing environment

To view corrosion engineering in its proper perspective, it is greatly necessary to consider that the choice or design of materials heavily depends on many principles, as shown in Fig. 9(a), which includes its corrosion behavior. Moreover, corrosion resistance depends on kinds of factors as well, which requires a comprehensive knowledge of several fields as indicated in Fig. 9(b). The selection, design, and fabrication of metallic materials in Cl^{-}-

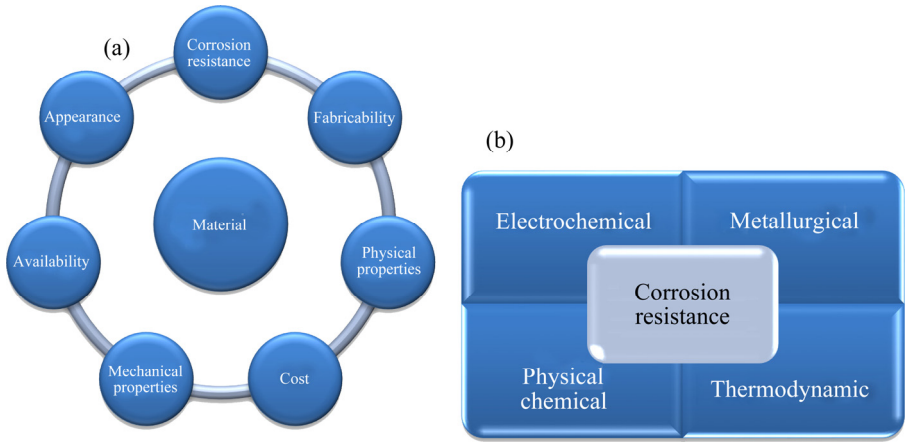

Fig. 9 Principles on selection or design of engineering material (a), and factors affecting corrosion resistance of metal (b)

containing environment have become one of the most active research areas recently.

All we all known, the corrosion of bi-phase or multiphase alloys is higher than that of homogeneous solid solution alloys with high purity due to the micro-galvanic corrosion acceleration effect caused by the second phases on the premise that the second phase is more cathodic than the metal matrix in the corrosive environment. Among the bulk metallic materials, the instinct noble metals (i.e., Ag, Pt, Au) possess superior corrosion resistances. However, pitting corrosion may still occur. Meanwhile, the poor mechanical properties and high costs restrict their applications widely. So far, numerous studies have been focused on the corrosion behaviors of traditional corrosion resistant materials (i.e., stainless steel (SS), nick-based alloy, Al alloy, and Ti alloy) and design of novel corrosion resistant materials (i.e., high entropy alloy (HEA)) by adding beneficial alloying elements (such as Cr, Ni, Mo, Cu) which are necessary for enhancement of the pitting corrosion resistance [31−35]. Among these alloying elements, Cr is one of the primary elements that play a major role in corrosion resistance of SSs. The galvanic series of various metallic materials in Sanya seawater in China were studied by CHEN et al [36]. They found that the galvanic series order from low to high was aluminum anode, aluminum alloy, cast iron, carbon steel, low alloy steel, copper alloy, martensitic SS, ferritic SS, pure copper and austenitic SS, duplex stainless steel (DSS) and nickel alloy. Pure copper and Al bronze had good corrosion resistance in Sanya seawater. Comparison of partial galvanic series is shown in Fig. 10 [37]. The corrosion resistances of the metallic materials mentioned above in 3.5 wt.% NaCl solution are shown in Fig. 11 [38]. In the case of pitting corrosion resistance in marine environment (South China Sea), 825 Ni-based alloy performed better than DSS (i.e., 2507 DSS and 2205 DSS), with SS like 317L and 316L the worst [39]. It should be noted that the pitting corrosion resistance of martensitic carbon steel could be improved by heat treatment due to the beneficial role of interstitial carbon atom [40].

In general, the welding properties of Al and Cu alloys are poor, especially in the case of dissimilar metals welding. The corrosion resistance of the martensitic SS in seawater is not satisfied, and the pitting corrosion resistance of ferritic SS is much worse than austenitic SS owning to Cr-depletion at grain boundary. Therefore, 316L austenitic SS and DSS (i.e., 2205, 2507) are extensively used in offshore structures for many decades [41]. 8200

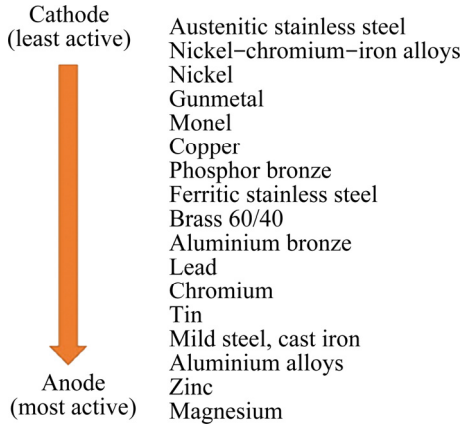

Fig. 10 Comparison of galvanic series of metals [37]

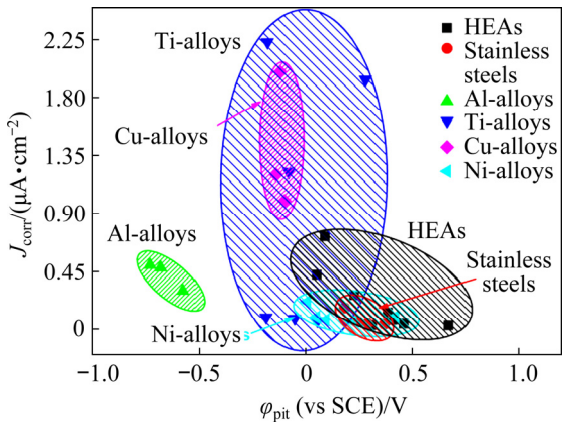

Fig. 11 Overview diagram of corrosion resistances of metallic materials based on corrosion current density (J_{corr}) and φ_{pit} in 3.5 wt.% NaCl solution [38]

tons of DSSs were used for the Hong Kong—Zhuhai—Macao Bridge with a design service life of 120 years. As mentioned above, the superior corrosion resistance of DSS is attributed to the namometer-thick passive films on its outer surface. DSS has a two-phase microstructure comprising approximately equal phase fractions of ferrite (α) and austenite (γ). However, the interaction of Cl^- with the passive films on the α and γ phases of the DSS was different from each other. Cl^- attacked the outmost surface of the passive film on α phase and the interface of passive film/γ [42]. Once the passive oxide film was breakdown by localised attack, a small area of the metallic substrate was exposed to the Cl^--containing environment. Then, this pit acted as an anode compared with the contact interface. Although there existed galvanic corrosion between α phase and γ phase due to the potential difference, it benefited the passive behaviors of both phases in DSS [43].

Grain refinement is commonly used to improve the mechanical properties of bulk metallic materials, according to the Hall−Petch relationship. Additionally, when the metallic materials show oxide/passivity behaviors in active media, there is also a relationship between average grain size (d) and corrosion rate (R_{corr}), which is summarized to be analogous to the Hall−Petch relationship as follows [44]:

$$R_{corr}=A+Bd^{-0.5} \quad (6)$$

where A and B are constants. It had been proved by CHENG et al [45] that the finer the grains or phases are, the more significant the galvanic effect between the two-phases in DSS is, then the stabler the Cr_2O_3-rich passive films on them are and the higher the corrosion resistance is. While, in the case of annealed and hot-rolled low-alloy steel [46], 316L SS [47] as well as the as-extruded Mg alloy [48,49], coarse grains were proved to be beneficial to the corrosion resistance. It is known that grain boundary, which is a planar defect and has a higher energy than the surrounding crystal, increases with grain refinement. The high-energy grain boundary, especially the high-angle grain boundary, is prone to act as potential site and active pathway for pitting corrosion and be corroded preferentially [47,50]. Throughout the available literature, the effect of grain size on the corrosion performance is controversial, which needs to be clarified regarding of the type and the processing of metallic materials [51]. Besides, the inclusions such as sulphides (i.e., MnS), oxides, nitrides and high temperature precipitation of carbides or sigma (σ) phases, would induce pitting corrosion [19,52]. The density of inclusions correlates well with the density of pitting corrosion locations. Among these inclusions, MnS plays a critical role in the pit initiation. In details, the nano-sized $MnCr_2O_4$ particles embedded in MnS acted as cathode and promoted the dissolution of anodic MnS [53]. However, the micro galvanic corrosion could be greatly resisted by bathing the SSs in solutions containing Cu^{2+} [54]. Apart from these non-metallic inclusions, the Cu-rich phases in some newly developed SSs or DSSs would preferentially dissolve at the initial corrosion stage [19,55]. However, increasing the Cu content of grain-boundary precipitate could decrease the difference in potential of anodic sites and cathodic sites, subsequently decreased the galvanic corrosion rate [56].

Recently, the additive manufacturing (AM) emerged and rapidly developed to be a disruptive technology in a broad spectrum of industries worldwide. It was proved that the overall corrosion resistance of AM SS could be better than that prepared by conventional technology under proper parameters of printing process [57]. However, the intrinsic microstructural defects such as porosity (especially the irregular-shaped pores, also called lack of fusion (LOF) porosity), residual stress, and inclusions, which are susceptible to pitting

corrosion, are the drawback of AM and limit the great enhancement of corrosion resistance [58,59]. Greatly different from conventionally manufactured 316L SS, pit initiated and propagated from the LOF porosity in AM 316L SS is shown in Fig. 12 [59], which also indicated that the presence of occluded regions inside the LOF pores could have a strong influence on the pitting corrosion susceptibility in Cl^--containing environment.

Despite enormous experimental research has focused on the pitting corrosion, the localized attack is intrinsically of stochastic nature, and it is very hard to monitor the growth of pit in-situ and in real-time, so the computational models which can predict corrosion, in particular the pitting corrosion, and optimize the corrosion conditions can be a valuable complement. In recent years, various computational approaches including the finite element method (FEM) [60−62], peridynamic (PD) theory [63−66], phase-field formulation [67,68] and cellular automate modeling [69,70] were available to provide even better representation of the process of electrochemical corrosion. The simulated evolution of pitting corrosion of carbon steel based on FEM coupled with moving boundary mode is shown in Fig. 13 [60]. Mesh presentation of boundaries in the two-dimensional model, which is also the cross-section of boundaries in the three-dimensional (3D) model, is shown in Fig. 13(a) for the numerical simulation of pitting corrosion of SS in NaCl solution. The green and black lines were the active boundaries, the blue carved line represented the bulk solution, whereas the red lines were the inactive regions. Since the model was axial symmetry geometry, it was changed by removing half of the original region along the line of symmetry, as shown in Figs. 13(b−g), which revealed the movement of boundaries of a pit and also the level of concentration of Fe^{2+} with time increasing. The pit grew deeper as time passed. After 40000 s (≈11.11 h), the geometry of the pit was illustrated to be a deep trough of depth around 4.5 μm [60]. However, this model needed to be validated by direct experimental evidence. Vividly, realistic pit morphology of SS tended to grow under perforated lacy covers. A new 3D model based on PD theory with a hemispherical initial pit was developed by

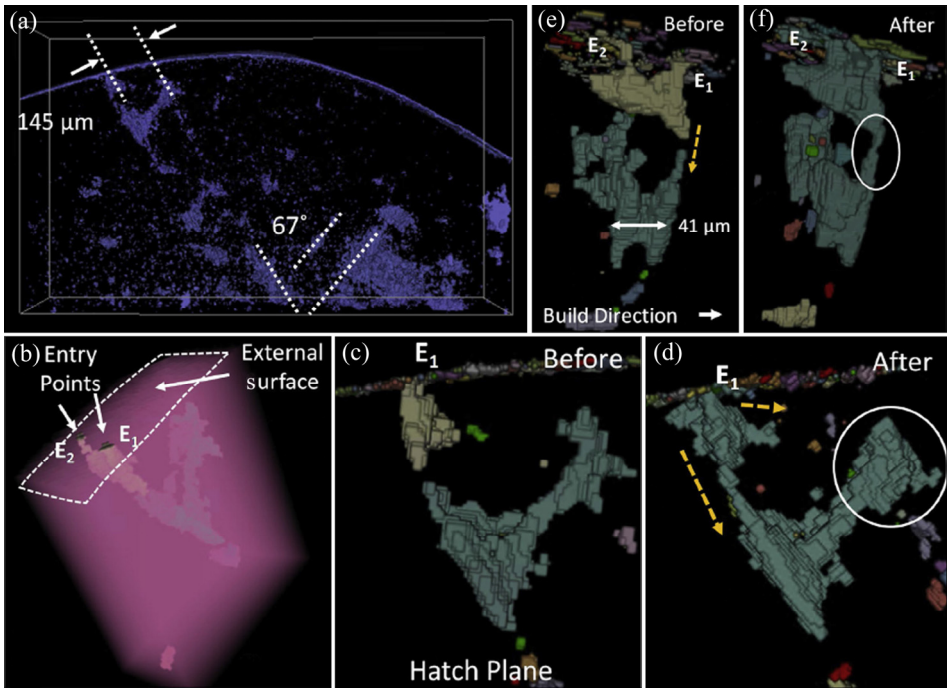

Fig. 12 Development of corrosion within LOF structure from volumetric reconstructions of P125-S600 specimen before (a, b, c, e) and after (d, f) one-week immersion into ferric chloride solution: (a) General overview of region containing target LOF structure along with other LOF structures; (b) External surface indicated by dashed white line (The entry points into the LOF structure are also indicated by the labels E1 and E2); (c, d) LOF structure prior to and after corrosion, respectively (only entry point E1 can be seen from this perspective); (e, f) LOF structure within powder bed plane before and after corrosion [59]

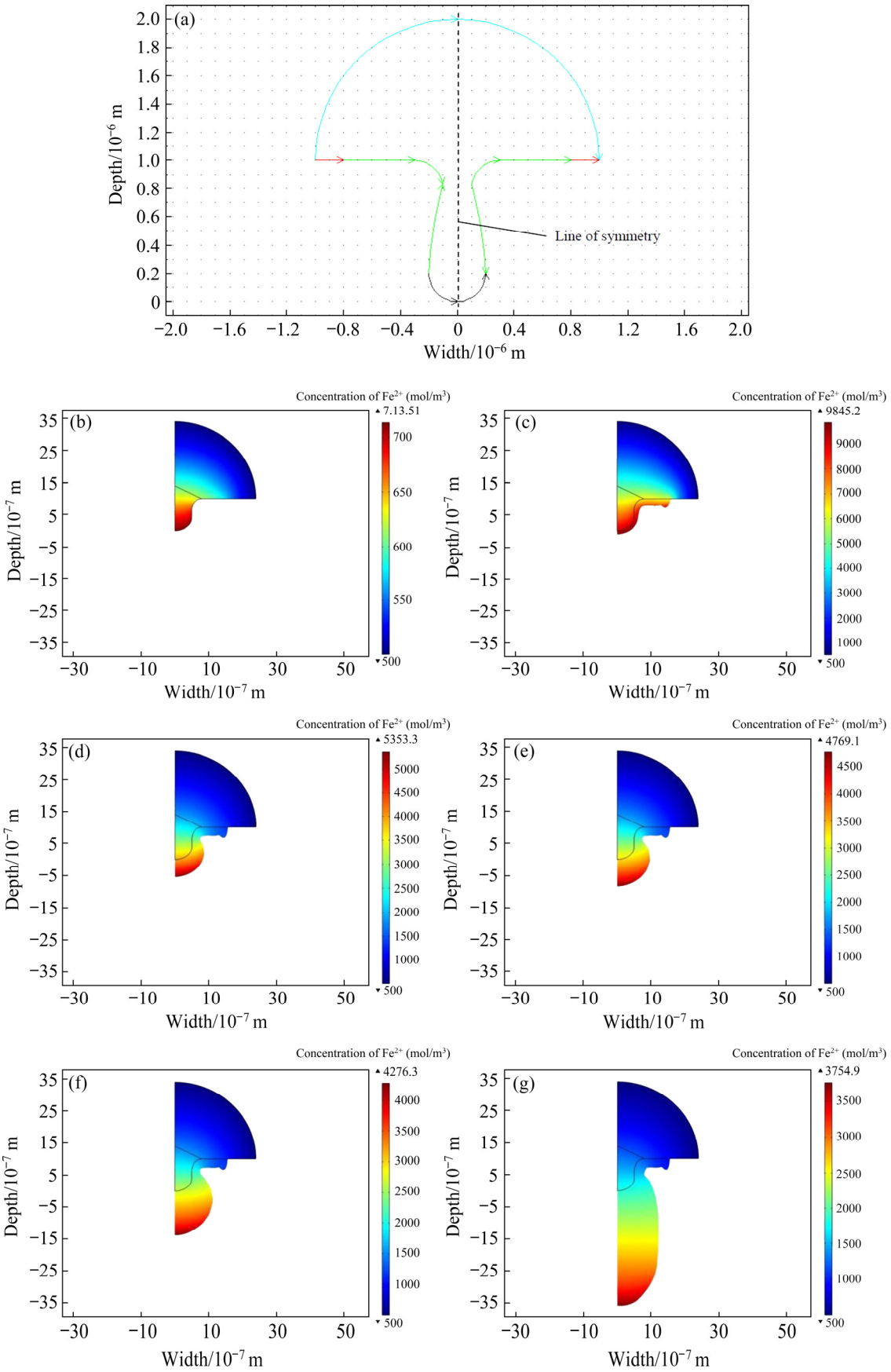

Fig. 13 Simulated evolution of pitting corrosion of carbon steel based on FEM coupled with moving boundary mode [60]: (a) Mesh presentation of boundary model; (b) 400 s; (c) 1000 s; (d) 3000 s; (e) 5000 s; (f) 10000 s; (g) 40000 s

BOBARU et al [63−65] and ROKKAM et al [66] to simulate the pitting corrosion of SS in NaCl solution, which was greatly in agreement with the experimental results, as shown in Fig. 14 [63].

It has been proven that the synchrotron radiation X-ray computed microtomography (SR-μCT) technique is also a more effective approach for 2D and 3D non-destructively analysis of microstructure with a resolution of the order of a micron compared with conventional methods. Time-lapse 3D (called 4D) imaging could be created by the SR-μCT with high brightness [71]. ALMUAILI et al [15,72] used a quasi in-situ X-ray computed tomography test to study the pitting corrosion kinetics of 304L SS in NaCl solution. The reconstructed 3D view of pit is shown in Figs. 15(a, b) [15,72]. The pit 1, pit 2 and pit 3 were formed after the first and second polarization respectively, and the effects of time on (pit depth)^2 of the three pits are shown in Fig. 15(c) [15,72], which indicated that the pit growth followed the diffusion controlling law accounted for a linear

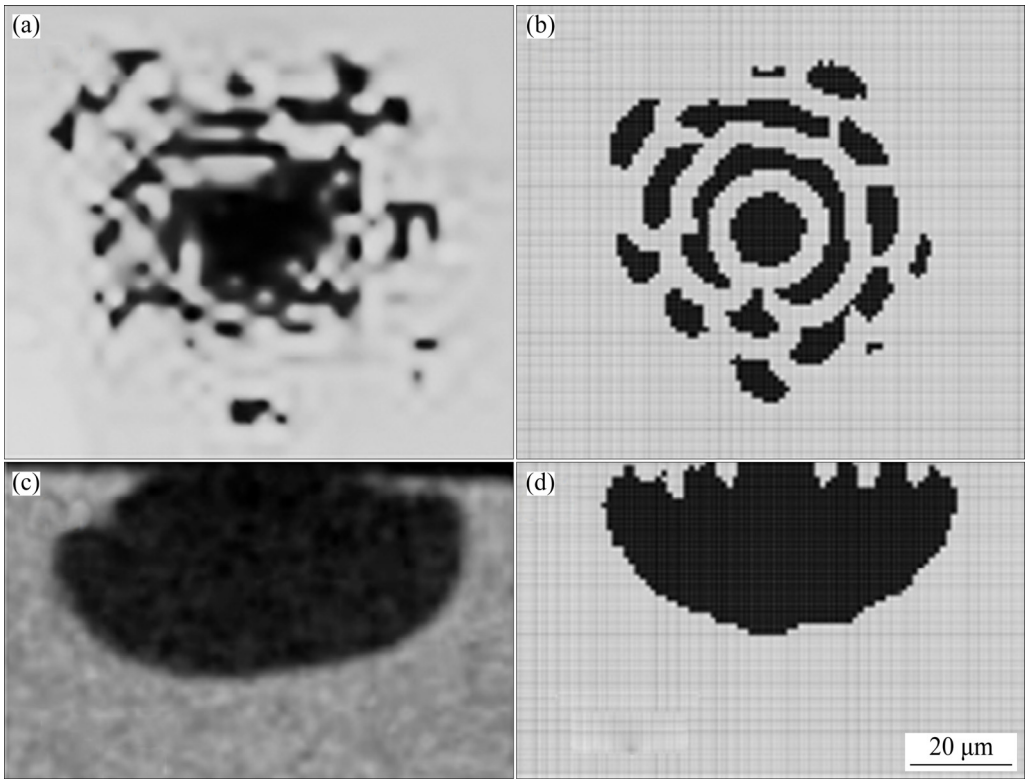

Fig. 14 Experimental (a, c) and PD simulation (b, d) results for pit grown in 304L SS and its lacy cover after 83 s of polarized corrosion in NaCl solution from top view (a, b) and cross section (c, d), respectively [63]

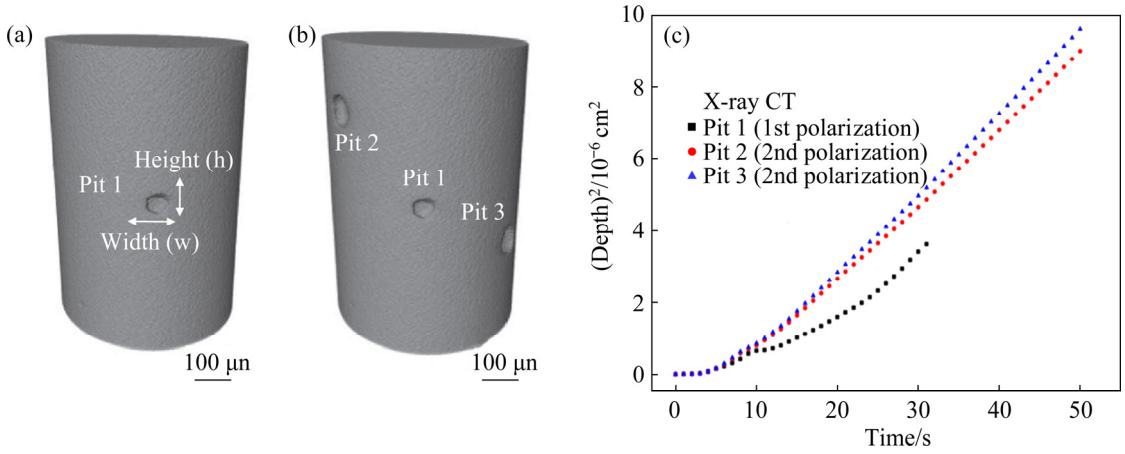

Fig. 15 Reconstructed X-ray CT data volume of wire after the 1st electrochemical polarization scan (a) and after the 2nd potentiodynamic polarization scan (b), and effect of time on (pit depth)^2 (c) [15,72]

relationship between square depth of pits and time.

Presently, HEA, as a new type of alloys, has attracted considerable attention of researchers in the field of materials owing to its excellent corrosion resistance as well as other superior properties (mechanical properties and wear resistance) [38]. Accordingly, some HEAs with high corrosion resistance even better than SSs in Cl^--containing environments were developed [37]. In general, a dual-layer passive film consisting of metal-oxide and $Cr(OH)_3$ was formed when the HEAs were exposed to the corrosive solution [73]. In particular, it was reported that the corrosion resistance of a CoCrFeMnNi HEA fabricated by AM outperformed that of the as-cast HEA with the same composition due to grain refinement and homogeneity of AM-HEA. Nevertheless, the Cr-depleted zone in HEA was susceptible to the attack of Cl^- and significantly reduced the pitting resistance in Cl^--containing environments [74].

However, the DSS is the most expensive steel, and the cost of HEA is high, and its preparation process is also extremely complex, so developing new materials or technology with high corrosion resistance and low cost is on the way.

3 Surface treatment for improving corrosion resistance

Although the corrosion of metallic materials was unavoidable, it could be minimized by different types of protective methodologies (inhibitors [75,76], metal-polymeric coating and epoxy coating [77−79], thermal metal spray [80,81], surface alloying [82,83], hot dipping [84−86], photoelectrochemical cathodic protection [2,87], etc.) to retain the mechanical properties. Compared with the bulk metallic substrate, the surface treatment to improve the corrosion resistance was more effective and convenient. Surface treatment for corrosion protection must offer an effective physical barrier, impeding the access of aggressive species like Cl^- to the metal substrate. There were various kinds of surface treatment. Taking the chromate-rich passivation treatment and/or primers and pigments based on chromates for example, the anti-corrosion mechanism of chromate treatment was the formation of protective oxides film. However, it was strictly prohibited due to its environmentally unfriendliness. Therefore, the present review focused on the most recent trends on "green" corrosion protective surface treatment based on these two categories as follows.

3.1 Organic coatings

Among the anti-corrosion coatings, organic protective coatings are the most widely used. At present, the single-layer or multi-layer graphene films on the surfaces of metal substrates attracted large attention [78,88]. Once the diffusion of water molecule via such anti-corrosion coatings, the adhesion of the coatings would be reduced, which subsequently resulted in the delamination. Some even focused on the graphene-modified organic anti-corrosion coating [78]. However, the graphene organic anti-corrosion coatings have not yet formed mature products or have been widely practical applications. Meanwhile, since organic coatings are easy to age, especially in the sunlight, their maintenance costs are high, which adds up to more than 60% of all anti-corrosion expenditures [6].

The surface features of lotus leaves give a clue that utilizing the superhydrophobicity to avoid the corrosion of metal substrates. The anti-corrosion mechanism of nature-inspired superhydrophobic coatings is attributed to both effects of the existence of hydrophobic molecules and trapped air that play a role of physical barriers against corrosion and prevent the active aggressive ions contacting the underlying metal surface. Some super- hydrophobic surfaces even reveal superior self- cleaning performance [89,90]. Overall, kinds of functional and smart coatings emerge endlessly [91].

However, the thickness of the coating is relatively thin, and its density and integrity are difficult to guarantee, in particular, in large-scale construction, resulting in failure to deliver long-term corrosion protection against Cl^- attack. Corrosion often preferentially starts from defects, such as pores, cracks and inclusions. At the same time, the presence of non-protective films such as oxides/hydroxides on the surface of metal substrate will weaken the bonding force between the coating and the substrate. Hence, corrosion media such as Cl^- easily penetrate the coating through these defects in the coating and accumulate at the coating/metal substrate interface, resulting in delamination of the coating and subsequent failure and the corrosion of the underlying metals [89,90]. Meanwhile, the preparation processes of some

coatings are very complex and their costs are high, and organic coatings also suffer from aging (less than 7 years). In addition, the organic coatings coated on the noble metal outperform similar coatings coated on the less-noble metal when it is used to prevent galvanic corrosion. Therefore, the combination of organic coatings and cathodic protection is considered to be the most economical and effective protection method.

3.2 Metal and its alloy or compound coating

The anti-corrosion mechanism of metal and its alloy or compound coating is mainly considered on the effective galvanic protection by sacrificial anode, self-healing properties against local damages and physical barriers, which are associated with their passive nature. Thus, the potential of protective coating must be much more negative than metal substrate. Commonly used sacrificial anode coatings are Zn-, Al- and Mg-base. The performance of some of the metal coatings has been proven in both laboratory and field studies. However, the anodic dissolution of Mg-base resulted in the formation of H_2, which is harmful for the coating. Among Zn-based and Al-based coatings, the Al−Zn alloy coatings (Zn−55wt.%Al−1.6wt.%Si) show the best corrosion resistance especially in the Cl^--containing environments. Other elements (e.g. Mg, Si, and RE) have an important effect on the corrosion resistance of Al−Zn coatings [92−96]. In general, the corrosion stability of quaternary Zn−Al−Mg−X alloy coatings outperformed binary Zn−X and Zn−Al−X and Zn−Mg−X coatings [97].

The corrosion behavior of Al−Zn−Si−RE coating prepared by arc spraying was studied by JIANG et al [80]. They found that sacrificial anodic protection of the Al−Zn−Si−RE coating played a dominant role in improving the corrosion resistance in NaCl solution. The corrosion products mainly comprised simonkolleite [$Zn_5(OH)_8Cl_2·H_2O$], zinc aluminum hydrotalcites (i.e. [$Zn_6Al_2(OH)_{16}CO_3·4H_2O$] and aluminum chloride hydroxide hydrate [$Al_5Cl_2(OH)_{12}·4H_2O$] were deposed in defects and hindered further corrosion [80]. [$Zn_6Al_2(OH)_{16}CO_3·4H_2O$] is one of the layered double hydroxides (LDHs) [98], besides the Zn−Al LDH, there are kinds of others LDHs, such as Mg−Al LDH, Ni−Al LDH, and Fe−Al LDH. LDHs are a class of synthetic anionic clays that consist of positively charged layers containing alternatively distributed divalent and trivalent cations in the sheets and charge balancing anions between the layers [99]. LDH is also a smart anion-exchanger, and has a high affinity for Cl^- resulting in acting as Cl^- scavengers. LDH nanocarriers loaded with corrosion inhibitors could entrap the harmful aggressive Cl^-, accompanied with a triggered release of anionic corrosion inhibitors. Subsequently, the concentration of Cl^- in the corrosion media decreased and a corrosion inhibitor protective layer formed on the surface of the metal substrate, as shown in Fig. 16 [100,101]. Meanwhile, the oriented LDH films also exhibited better superhydrophobic behavior and acted as a protective barrier against corrosion attack.

Another method of producing Al−Zn (or Zn−Al) alloy coating was hot-dipping. Hot-dipping coatings were of great significance in protecting metal from corrosion. After hot-dipping aluminum, typical three-layer structures (top residual Al layer, middle Fe−Al intermetallic compound (IMC), and metal substrate) were represented. In general, the corrosion rate of Zn-based coating is much

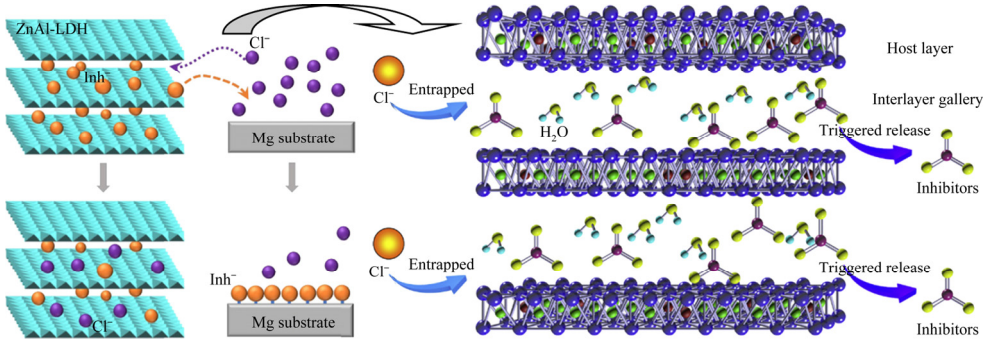

Fig. 16 Schematic representation of entrapment of aggressive chloride ions and triggered release of anionic corrosion inhibitors from LDHs [100,101]

smaller than that of cold-rolled steel, while the corrosion rate of Al−Zn (−Mg) coating is much smaller than that of hot-dip galvanizing [102]. Meanwhile, due to the large dissolution rate of the Zn layer in the natural water environment, the price fluctuation of Zn and the excessive consumption of Zn resources, hot-dipping Al−Zn alloy is replacing hot-dip galvanizing as a new type of anti-corrosion method in recent years. However, it raises one more related problem: Fe/Zn or Fe/Al dominates the interfacial reaction during hot-dipping Al−Zn (or Zn-Al) alloy, which had been explicated in our other research results [103].

In general, Al alloy does not provide sufficient sacrificial protection to steel due to the formation of a protective oxide film on the surface. However, this oxide film can be drastically attacked when subjected to severe marine environments, resulting in the effective sacrificial protection provided by the newly exposed surface. LIU et al [94,95] studied the corrosion resistance of hot-dipped Al−Zn−Si−*x*Mg (*x*=0, 1, 2.5, 3, 4 wt.%) in 3.5 wt.% NaCl solution, they found that 50.9Al−44.5Zn−1.4Si−3.0Mg coating exhibited the highest corrosion protecting, which benefited from the delay of pitting corrosion by the presence of $MgZn_2$ and Mg_2Si phases. Schematic of the galvanic corrosion of hot-dipped Al−Zn−Si−*x*Mg coatings in 3.5 wt.% NaCl solution is shown in Fig. 17 [94,95]. For the Al−Zn−Si coating, the corrosion process was divided into three stages: (1) At the initial stage, Cl^- broke the surface passive oxide film; (2) Al-rich phase played a cathodic protection role, and Zn-rich phase and Zn−Al eutectic phase were dissolved stably; (3) When the Zn-rich and Zn−Al eutectic phases were completely corroded, the Al-rich phase started to dissolve and formed galvanic corrosion with the IMC layer to accelerate the corrosion reaction. While for the Al−Zn−Si−3Mg coating, the corrosion was divided into four stages with the first stage same as that of the Al−Zn−Si coating. Secondly, Mg_2Si phase played a role of cathodic protection owning to its more electronegativity than Zn-rich phase. Then, corrosion of Zn-rich phase was the dominate corrosion reaction, and the corrosion product (Zn−Al LDH) of Zn−Al coating acted as barrier and inhibited mass transmission. At last, when the Zn-rich phase was completely consumed by corrosion, the corrosion of the Al-rich phase became the dominate corrosion reaction [94,95].

The optimum content of Mg in the hot-dipped Zn−Al−Si coating is found to be conflicting results

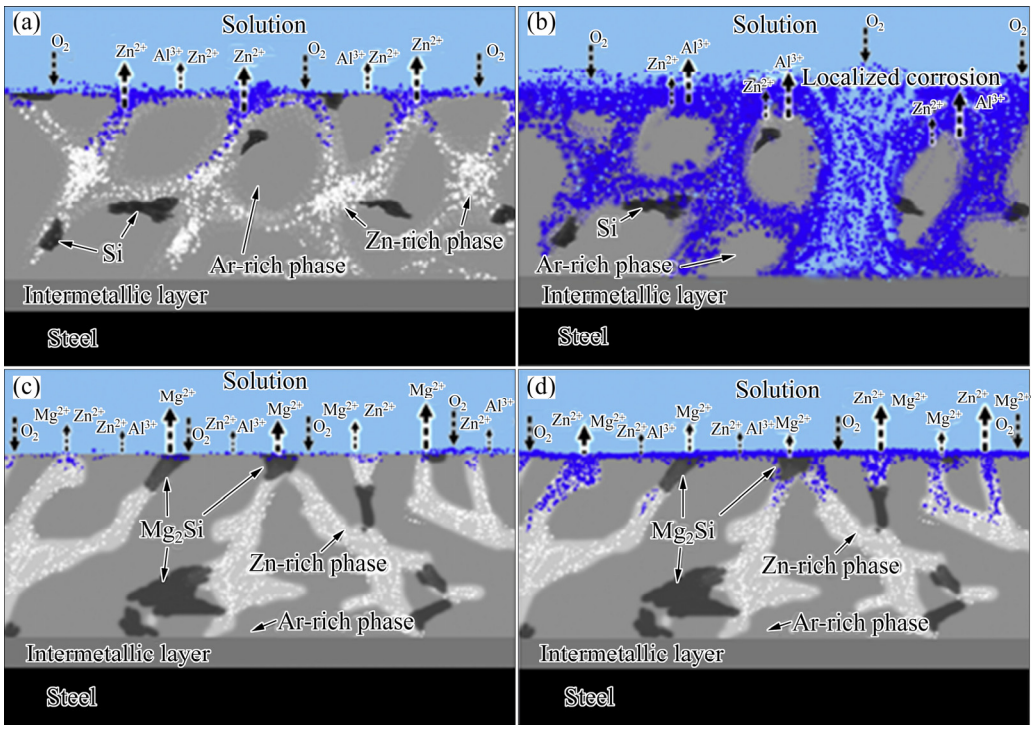

Fig. 17 Schematic of galvanic corrosion of hot-dipped Al−Zn−Si−*x*Mg coatings in 3.5 wt.% NaCl solution [94,95]: (a) Al−Zn−Si coating at stable stage; (b) Al−Zn−Si coating at accelerated stage; (c) Al−Zn−Si−3Mg coating at initial stage; (d) Al−Zn−Si−3Mg coating at stable stage [94,95]

in literature. LI et al [92] studied the effects of Mg addition (0, 0.5, 1.5, 2.5 wt.%) on the corrosion resistance of Galvalume coating (Zn−55Al−1.6Si) by neutral salt spray (NSS) test. They found that the corrosion resistance of Zn−55Al−1.6Si coating could be enhanced by Mg, and Zn−55Al−1.6Si−1.5Mg coating performed the highest anti-corrosion property. This difference may be caused by different experimental procedures. However, it was confirmed that alloying element of Mg benefited enhancement of the corrosion resistance of the hot-dipped Al−Zn alloy coating.

From the hot-dipped pure Zn and Zn−Al alloy to hot-dipped pure Al, the evolution of seawater corrosion products is shown in Fig. 18 [104]. These corrosion products, especially LDH, were deposed at the front of the corrosion interface and acted as a physical barrier to the corrosion process. However, there were only the corrosion products of the outer coatings, and the corrosion products of IMC layers did not appear because there was no metal substrate element (i.e., Fe) in the corrosion products. On the other hand, corrosion front did not reach the IMC layer.

As mentioned above, there was an interfacial reaction layer consisting of IMC after hot-dipping, and this IMC layer was supposed to have an influence on the corrosion behavior of the hot-dipping coating in Cl^--containing environments. However, little research focused on this, and the corrosion failure of this IMC layer was rarely reported [105]. It was inferred that the corrosion test was terminated before the corrosion media such as Cl^- reached the IMC layer due to the slow corrosion rate and the presence of the outer thick coating. It is known that the IMC (i.e., Fe−Al or Fe−Zn IMC) possesses outstanding corrosion resistance in Cl^--containing environments [106], so to study the corrosion behavior of Fe−Al/Fe−Zn IMC layer formed during hot-dip aluminizing/galvanizing, the outer Al/Zn layer should be consumed. However, whether there is a coupling effect between coating and IMC layer during the corrosion of metal substrate is still unknown.

An outer fully IMC phase was prepared by heat treatment of Zn−Mg−Zn multi-layer coated steel and its corrosion resistance in Cl^--containing environments was four times greater than that of the electro-galvanized steel [107], which was also proved by other researchers [85]. During the subsequent thermal diffusion treatment, the outer coating acted as Al source, with part of it remelting and oxidation, transformed into Fe−Al IMC, resulting in the thickness of IMC layer increased as the annealing time increased due to the inter-diffusion. Interestingly, a columnar grain structure developed after the thermal diffusion treatment, which only appeared in some special conditions [108−110].

4 Corrosion resistances of periodic layered structures in Cl^--containing environments

At present, the periodic layered structures (PLSs) are mainly prepared by eutectic/eutectoid reaction, surface deposition, and interfacial reaction including solid-state diffusion couple and hot-dipping.

4.1 Eutectic/eutectoid reaction

By controlling the cooling rate in the solidification or directional solidification under special compositions, the pearlitic microstructure consisting of alternating lamellae of two phases (also defined as PLS) or even fully PLSs in the

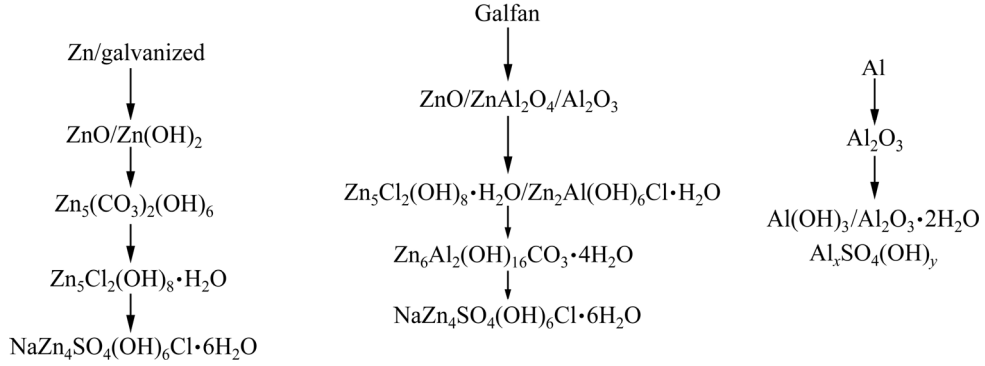

Fig. 18 Evolution of seawater corrosion products of different hot-dipped Zn−Al alloy coatings [104]

same direction can be produced by eutectic/eutectoid reactions. The PLSs distributed in the Mg alloy (AZ91) matrix benefited the enhancement of the corrosion resistance in NaCl solution [111−113]. It was worth mentioning that the types, morphology and distributions of PLSs had great influences on the corrosion properties of metal substrate. Compared to the other phases in Mg alloy, the PLSs were inert to corrosion attack (see Fig. 19 [111]) and acted as physical barrier and hindered the corrosion progression. It should be noted that the micro-galvanic coupling between metal matrix and PLS and that inside PLS coexist, even maintain a competing effect, which depends on the potential difference between each other. Enough electrochemical driving force is needed for the micro-galvanic corrosion between the layers, which ensures the valid cathodic protection for metal substrate. The predominated corrosion reaction inside the PLS occurred through micro-galvanic corrosion, resulting in the preferential dissolution of the α-Mg phase and undermining of the adjacent $Mg_{17}Al_{12}$ phase, which led to the corrosion degradation of PLS in NaCl solution in the form of "lamellar-type" (i.e., filiform corrosion) [111]. However, except for that produced by directional solidification, this kind of PLS is only randomly distributed in metal matrix. What's more, the position of PLS is very difficult to accurately control, and the width between mutually parallel laminae is on the scale of nanometer, which influences its anti-corrosion property, to some extent.

Another kind of PLSs is the fine nano-scale lamellar second phases with long period stacking ordered (LPSO) structure contained in Mg−RE (rare earth element)−TM (transition metal elements, such as Zn, Al, Ni). Up to now, 12 types of LPSO phases, involving 6H, 10H, 12R, 14H, 18R, 24R and other types, have been reported in Mg−RE−TM alloys and showed a lower corrosion rate, and acted as corrosion barrier [25,114−116]. However, the controvertible results about the order of preferential corrosion of α-Mg or LPSO phase still existed [117], which needs to be further explored.

4.2 Surface deposition

Nanolaminated Zn/Ni PLS coatings were developed by electrodeposition and showed better corrosion resistance than monolithic Zn or Ni

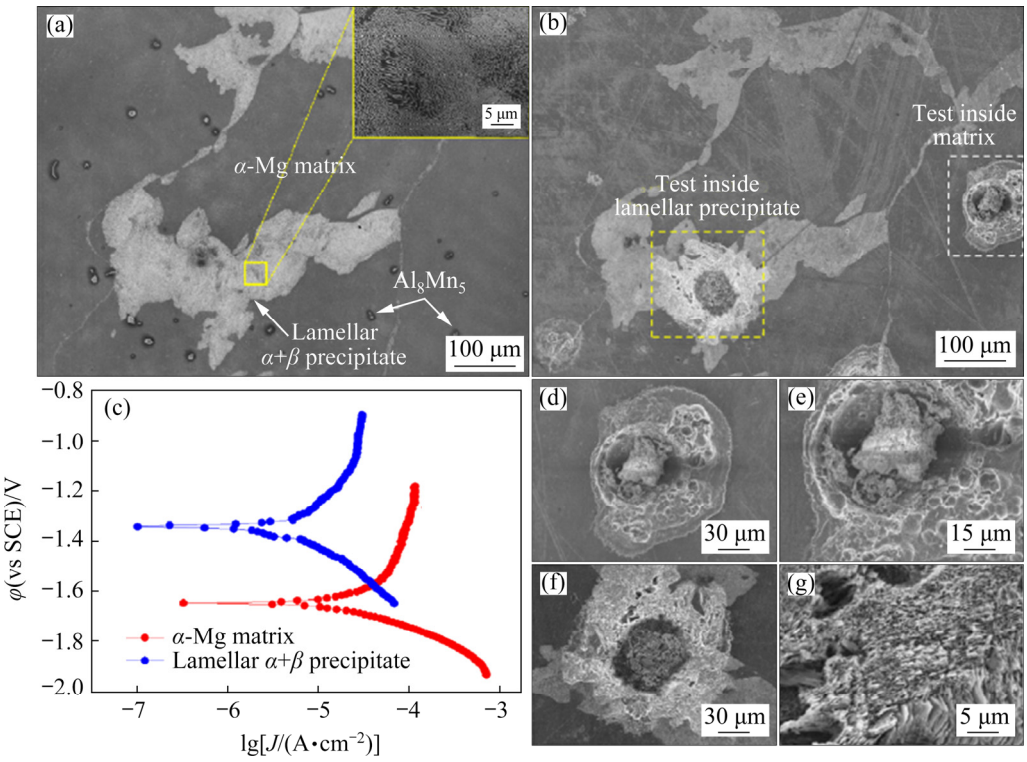

Fig. 19 Electrochemical microcell studies showing morphology of peak-aged alloy before (a) and after (b) testing, potentiodynamic polarization measurements of α-Mg matrix and lamellar at α+β precipitate in 3.5 wt.% NaCl solution (c), close view of corroded morphology after test inside α-Mg matrix (d, e) and inside lamellar at precipitate (f, g) [111]

coating with similar thickness in Cl^--containing environments. But the PLS was prone to delamination and then peeled from the substrate during the Cl^- attack [118,119]. Anti-corrosion capability of the PLS could be enhanced by optimized compositions, order and number of layers as well as 3D latticed structure [120−125]. In contrast with monolithic homogeneous coating, the time for corroding medium to penetrate through the PLSs coating to reach the substrate was much longer, which meant that the service life of the coating was prolonged under the same aggressive environment. The proposed corrosion penetration mechanism of PLSs coating was based on the galvanic interaction of alternately arranged more active (anodic) outer layer and noble (cathodic) inner layer. If the order of the layers was reversed, the corrosion protective performance would be reduced. Figure 20 shows the schematic illustration of the corrosion penetration mechanism: (1) Pit initiated from the outer anodic layer due to the local breakdown of passive oxide film caused by Cl^- localised attack. The anodic layer preferentially dissolved gradually during pitting corrosion, which resulted in the formation of pinhole. (2) As the pinhole reached the beneath cathodic layer, which was somewhat inert to corrosion attack acted as physical barrier against corrosion, corrosion propagated laterally along the anodic/cathodic interface rather than directly penetrating into the substrate. Eventually, the noble sublayer metal was exposed to the corrosive agent (Cl^-), corrosion cell with small anode and large cathode was produced, resulting in the accelerated dissolution of anodic layer. Meanwhile, a new pit was created at the defective location of cathode. (3) The electrical resistance between the edge of the remained anodic layer and the cathodic layer increased as anodic layer dissolved. Once it reached a critical value, cathodic protection effect decreased and consequently the corrosion of cathodic sublayer would initiate. (4) The pinhole penetrated throughout the cathodic sublayer until the fresh anodic underlayer exposed to the corroding medium and cathodic protection proceed again [121,124]. These repeated processes made the corrosion agent

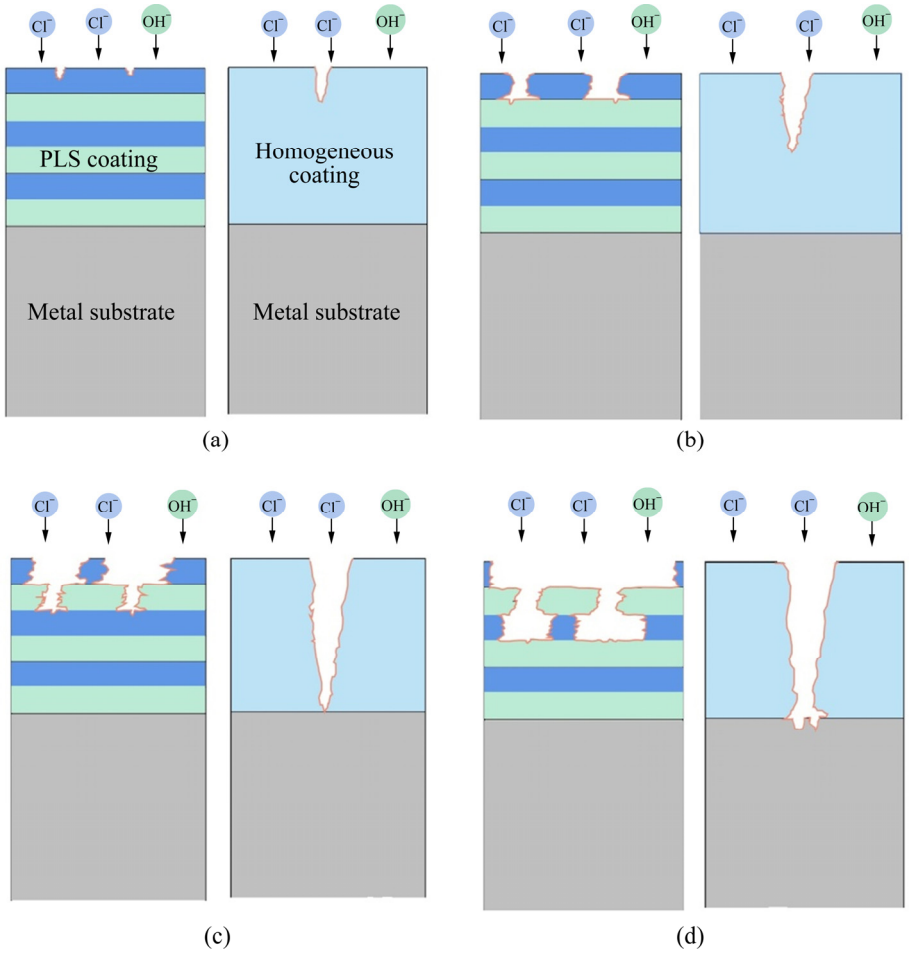

Fig. 20 Schematic illustration of corrosion penetration mechanism

path deflection from transverse direction to lateral direction, thereby improved corrosion protection was achieved. During the corrosion attack, most of the cathodic layers stayed in place except for some undermined and fallen out due to lack of supporting of the adjacent anodic layer which preferentially dissolved.

Note that another important aspect related to improved corrosion protection regarded the micro-structural heterogeneity of PLSs. Figure 21 [126] showed the simulated corrosion damages of PLSs with different arranging directions caused by the similar initial pit. Case A represented the arranging direction of PLSs parallel to that of the pit depth. On the contrary, Case B represented the arranging direction of PLSs perpendicular to that of the pit depth, as shown in Fig. 21(a). It was assumed that the corrosion resistance of Phase 1 was worse than that of Phase 2, thus, pit grew preferentially into Phase 1, which led to the pit depth of Case A much larger than that of Case B after the same corroding time, as demonstrated in Figs. 21(b) and (c). The corrosion behaviors of PLSs exhibited obvious corrosion anisotropy. The corrosion anisotropy also limited the anti-corrosion property of PLSs formed by eutectic/eutectoid reaction due to the random direction relationship between PLSs and pit depth. Thereby, the techniques that could control the formation direction of PLSs will significantly benefit the enhancement of corrosion resistance.

4.3 Interfacial reaction diffusion

As described in our previous work [127], PLS formed by interfacial reaction diffusion was different from that formed by eutectic/eutectoid reaction in two key aspects. First, the dominant arranging direction of this PLS was parallel to the reaction interface, while, that of the pearlitic was perpendicular to the reaction interface. Secondly, the formation mechanism was different: the former was generated by chemical reaction between diffusion couples. The thickness of PLS increased as reaction time increased, which caused long-range diffusion of components in diffusion couple. In contrast, the formation of pearlitic was due to the supersaturated precipitation of alloying elements (e.g. C), belonging to short-range diffusion [128]. Recently, PLSs formed at the $(Cr,Fe)_2B$/Al interface have been discovered during the hot-dipping aluminum of Fe−Cr−B cast steel, as shown in Fig. 22 [129]. The schematic of the formation of PLS by the interfacial reaction between $(Cr,Fe)_2B$

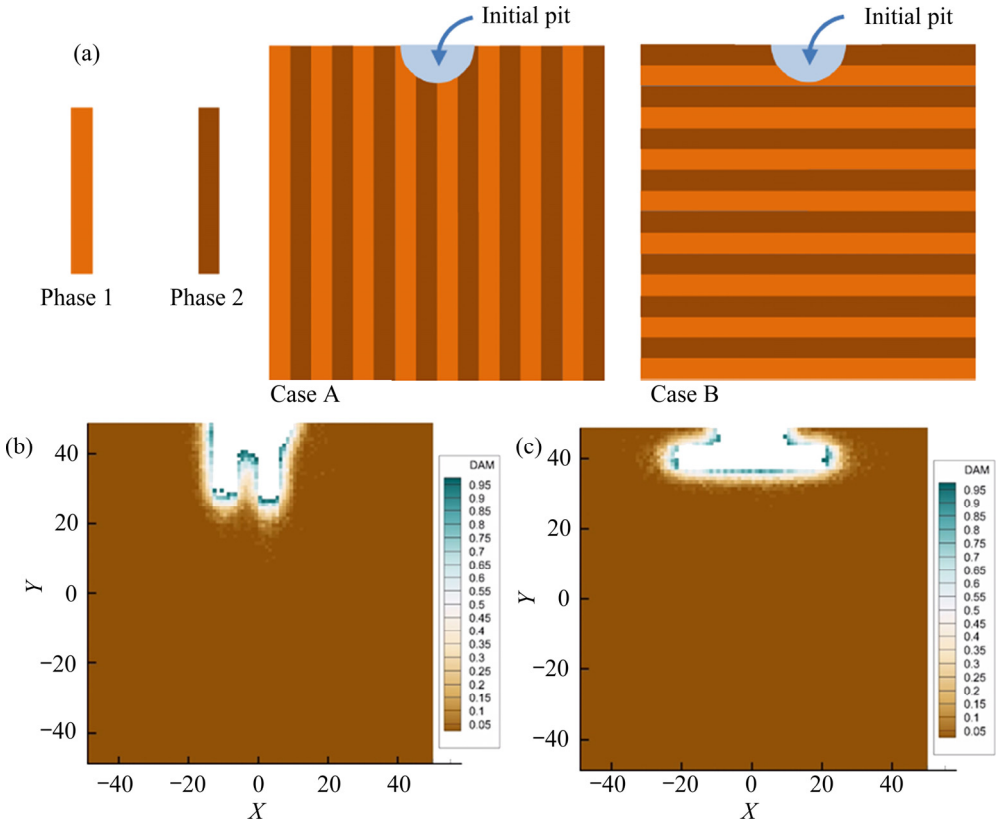

Fig. 21 Simulated corrosion damages of PLSs with different arranging directions caused by similar initial pit [126]

phase and molten Al was revealed by Fig. 23 [129]. When $(Cr,Fe)_2B$ phase came into contact with molten Al, inter-diffusion would take place. Due to thermodynamic instability and notable difference in solubility in Al melt, Fe atoms in $(Cr,Fe)_2B$ phase preferentially dissolved into molten Al. Interaction between the inward diffusion Al atoms and the Fe-depleted $(Cr,Fe)_2B$ occurred, which led to Cr−B−Al IMC phase forming. And its thickness increased with the reaction proceeding. Once the local thickness of IMC phase reached a critical value, a micro-crack initiated at the IMC/substrate interface. New Fe−Al IMC phase nucleated and grew along the micro-crack under the restraint of Cr−B−Al IMC phase with lamellar growth characteristics. Again, micro-crack originated once the critical thickness reached.

Apart from the essential role of Cr content in Fe−Cr−B cast in formation of PLSs, another important factor was considered to the Zn content in Al melt. Figure 24 [103] showed the schematic of both effects of Cr and Zn contents on the formation of PLS during the hot-dipping Al−Zn alloys of Fe−Cr−B cast steels, which demonstrated that PLS could only be produced in a special region bounded by the Cr content in Fe−Cr−B cast steel and the Zn content in Al−Zn melt. That was why no PLSs were formed when Fe−Cr−B cast steels were dipped into Zn melt containing no more than 0.3 wt.% Al. To the best of our knowledge, this is the first report that the critical transformation phenomenon of interfacial reaction dominated by Fe/Zn or Fe/Al can be depended on the visual PLS behaviors in Al−Zn alloy melts.

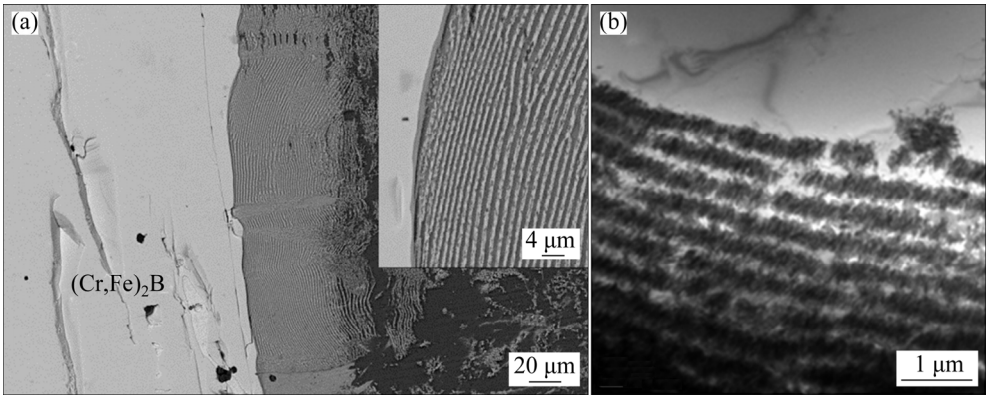

Fig. 22 Formation of PLSs at $(Cr,Fe)_2B$/Al interface (a), and bright field image of PLSs (b) [129]

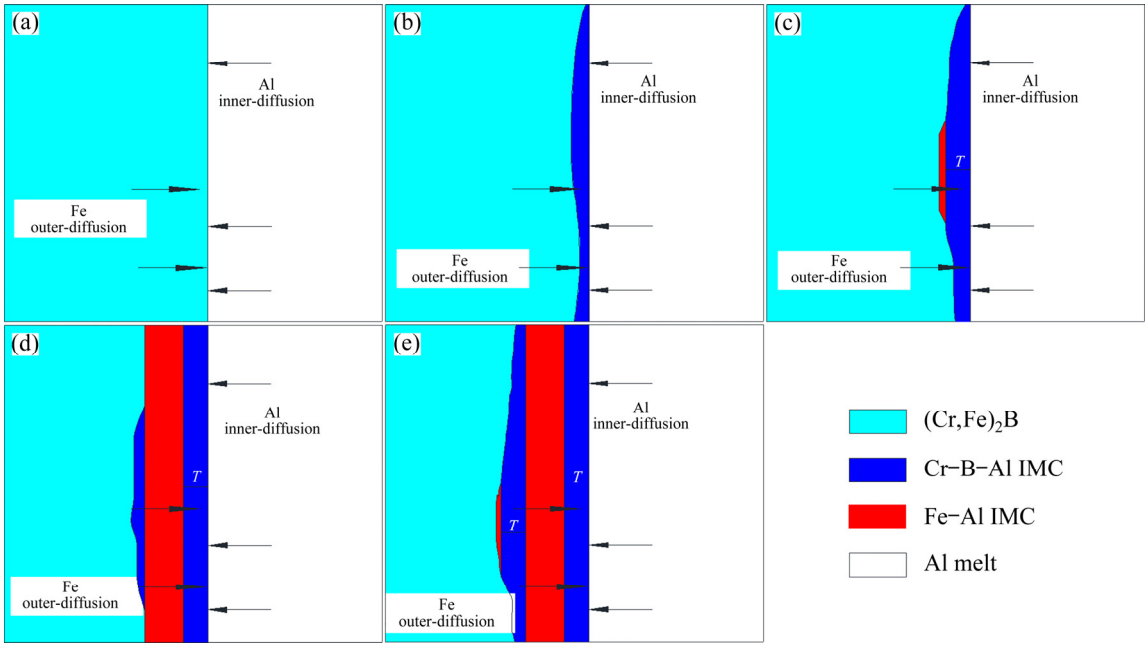

Fig. 23 Schematic of formation of PLS by interfacial reaction between $(Cr,Fe)_2B$ phase and molten Al [129]

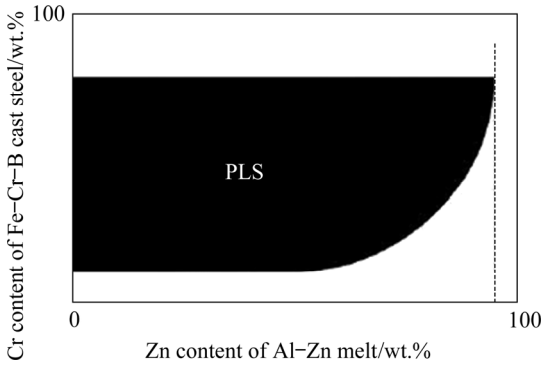

Fig. 24 Schematic of both effects of Cr and Zn contents on formation of PLS during hot-dipping Al−Zn alloys of Fe−Cr−B cast steels [103]

Moreover, in order to reproduce the process of PLS formation, synchrotron X-ray radiography experiment was carried out on BL13W1 beamline at Shanghai Synchrotron Radiation Facility (SSRF), China, as shown in Fig. 25. The sample of Fe−15.0wt.%Cr−4.6wt.%B cast steel used in the synchrotron radiation experiment was pre-treated by hot-dipping aluminum, where PLSs were formed during the hot-dipping aluminum. The sample with pre-formed IMC layer approximately parallel to the direction of X-ray was fixed by two Al_2O_3 ceramic plates, as shown in Figs. 25(a, b), followed by diffusion annealing (heated to (750±5) °C, held for 1 h, then cooled in the furnace). The microstructural

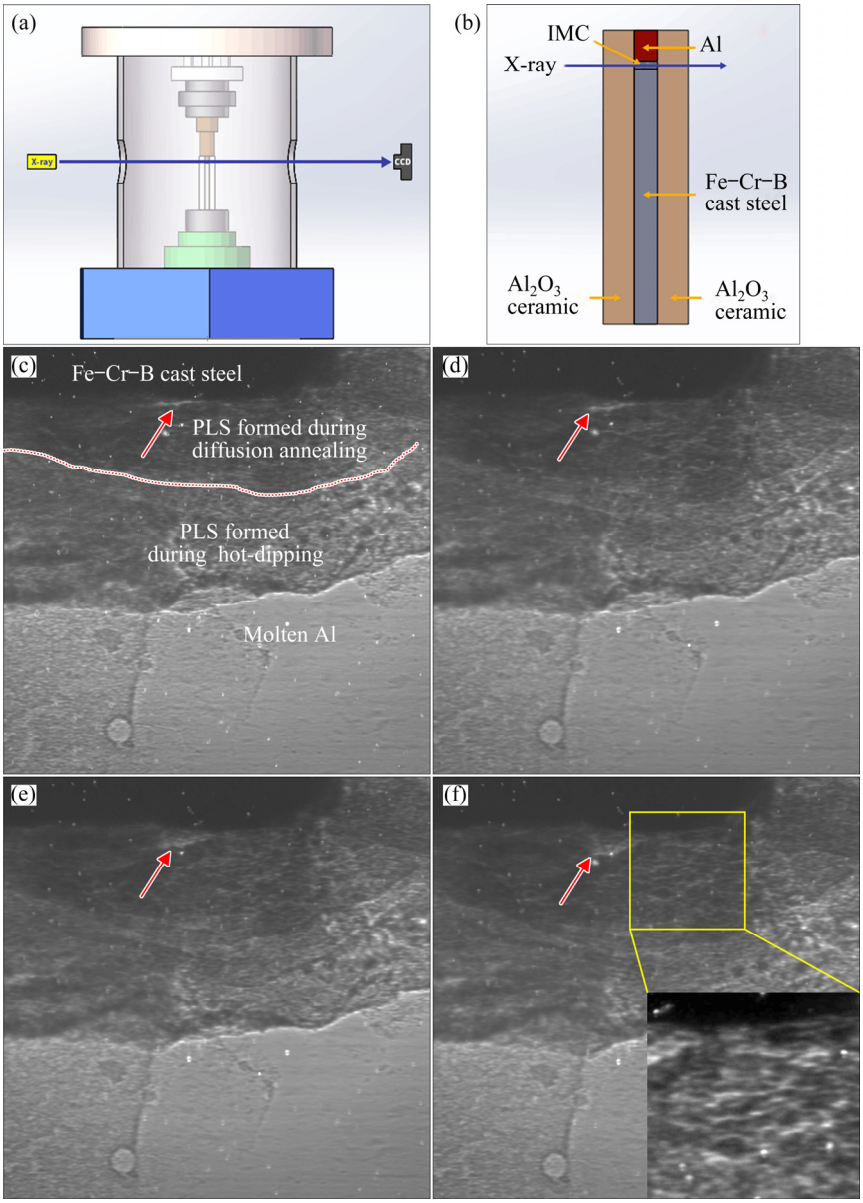

Fig. 25 Schematic of synchrotron X-ray radiography experiment carried out on BL13W1 beamline at Shanghai Synchrotron Radiation Facility (a, b), and microstructural evolution of PLSs during synchrotron X-ray radiography experiment at 50s (c), 1050 s (d), 2050 s (e), and 3050 s (f)

evolution of PLSs is shown in Figs. 25(c−f). It was obvious that the area consisting of PLSs between the white dot marked by the arrows and Fe−15.0wt.%Cr−4.6wt.%B cast steel thickened as the holding time increased.

Besides, the corrosion resistance of hot-dipping aluminizing-thermal diffusion treated Fe−15.0wt.%Cr−4.6wt.%B cast steel was also studied by immersion in 3.5 wt.% NaCl solution, and the corrosion morphologies are shown in Fig. 26. The corrosion direction was same as the Case A shown in Fig. 21(a). Compared with that before corrosion, the morphology changed obviously. The rust was evident and increased as the corrosion time extended.

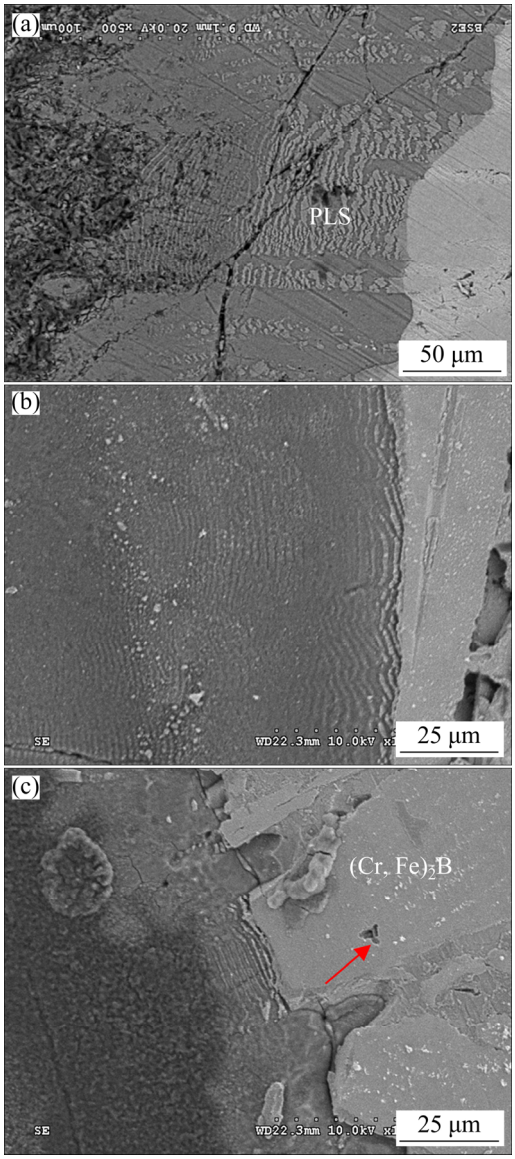

Fig. 26 Corrosion morphologies of hot-dipping aluminizing-thermal diffusion treated Fe−15.0wt.%Cr−4.6wt.%B cast steel after immersion in 3.5 wt.% NaCl solution for 4 h

The PLSs were still visible, while pitting corrosion appeared on the surface of $(Cr,Fe)_2B$ phase as indicated by the arrow in Fig. 26(c). Therefore, PLSs showed superior corrosion resistances. Further study on the corrosion behaviors of PLSs is on the way.

4.4 Additive manufacturing (AM)

Apart from the general applications in manufacturing complex bulk metal materials, AM can also be utilized for controlling crystallographic texture [57,130,131]. A unique texture called crystallographic lamellar microstructure (CLM) with two differently oriented grains alternately arranged in 316L SS was developed via AM. Furthermore, compared to commercial 316L SS, the CLM showed better corrosion resistance in NaCl solution [57]. Strictly speaking, this CLM is different from the PLS consisting of different phases as mentioned above, which is attributed to the same composition of the alternating layer with multiple crystallographic orientations in CLM. In fact, there also existed a strict orientation relationship between the alternating phases of PLS formed at the $(Cr,Fe)_2B$/Al interface. Thus, the underlying mechanism of enhanced corrosion resistance by CLM remained unclear. However, it can be referred to the hydrophobicity generated from the oriented surface or interface.

5 Corrosion-wear resistances of metallic materials in NaCl solution

As mentioned above, the generalized seawater corrosion was an extremely complex process involving corrosion, corrosion-wear and the synergistic effects of electrochemical corrosion and mechanical wear. By the way, wear can be in the forms of erosion, abrasion, sliding or fretting. Therefore, in addition to the real sea exposure test under full immersion condition with the physical attack of the wave, as shown in Fig. 27 [39], some simplified methods including erosion-corrosion, tribocorrosion with mechanical loading were used under laboratory conditions through NaCl solution during the past decade. Meanwhile, experiments on the corrosion-wear performances of metallic materials in NaCl solution were carried out subsequently.

5.1 Erosion-corrosion properties

Jet impingement methods with static samples have been widely used to investigate the erosion-corrosion properties of materials under high-velocity sand-containing solutions. It had been reported that both DSSs and super DSSs had superior erosion-corrosion resistance, which was attributed to their high hardness and the work hardening of γ phase under impingement [132]. The erosion-corrosion tests adopted by ARIBO et al [133] are shown in Fig. 28, except for the pure erosion, anodic polarized erosion was also carried out. They found that lean DSSs (UNS S32101 and 32304) had better resistance to pure erosion and erosion-corrosion than UNS S30403 SS. The deformation of subsurface and phase transformation

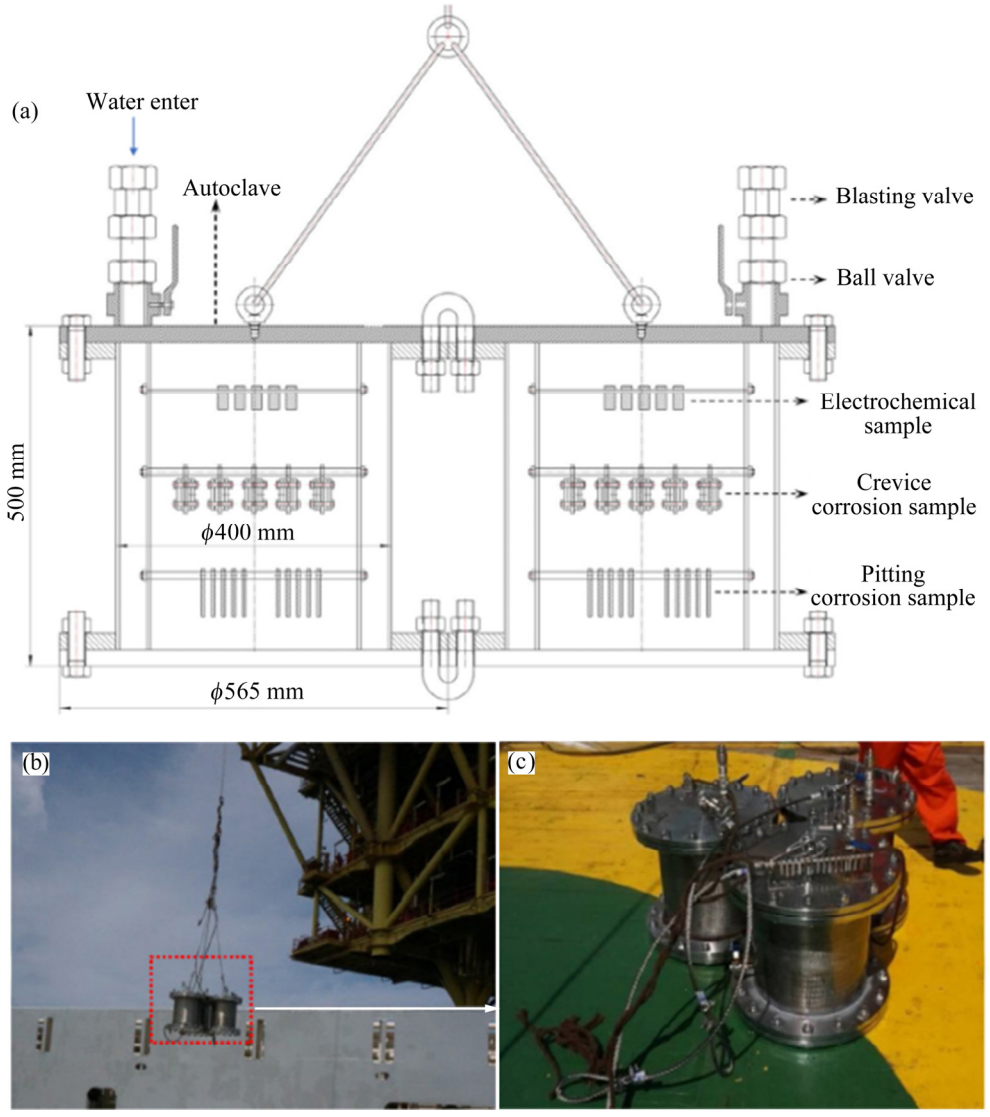

Fig. 27 Schematic diagram (a) and photos (b, c) of experimental setup for in situ marine corrosion experiments [39]

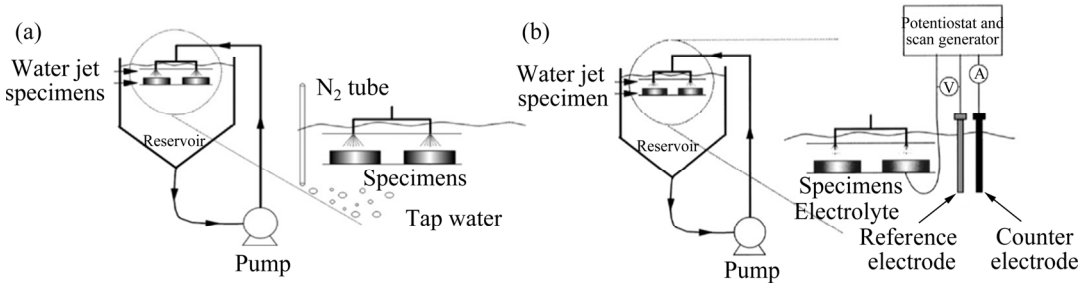

Fig. 28 Recirculating jet impingement rig: (a) Pure erosion; (b) Erosion-enhanced corrosion [133]

from γ to martensite caused by impact of the high-velocity sand-containing solution accounted for the improved performances [133].

Another type of erosion-corrosion apparatus with static sample was using loop system, as shown in Fig. 29(a) [134]. Samples were mounted at the elbow of pipelines which suffered from rather serious damage due to the great changes in flow direction and flow velocity (Figs. 29(b, c) [135]). The change in hydrodynamics at the elbow played an essential role in producing significant difference in erosion-corrosion behavior at different locations of elbow. ZENG et al [136] pointed out that the inhibition like thioureidoimidazoline could remarkably inhibit the anodic reaction, and the

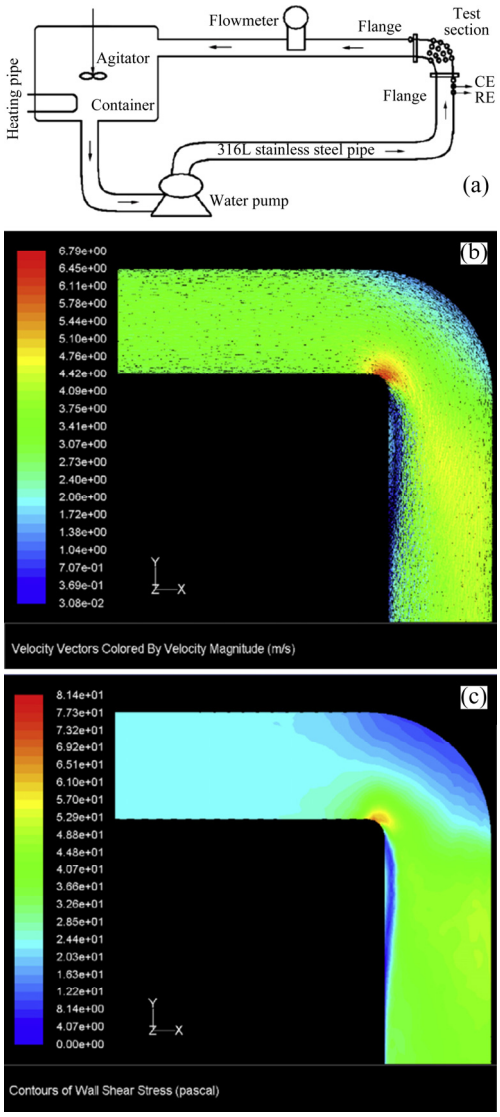

Fig. 29 Erosion-corrosion loop test system: (a) Loop test system [134]; (b) Fluid flow velocity distribution along elbow [134]; (c) Shear stress distribution along elbow [135]

inhibition efficiency at the inner wall was lower than that at the outer wall. However, this kind of erosion-corrosion test with static samples facilitates the electrochemical measurement, but it covers a large area.

In addition to the test with static sample, the secondary erosion-corrosion test was characterised by the rotating sample. JIANG et al [137] reported a simply modified erosion-corrosion test with rotating disc electrode specimens as shown in Fig. 30(a), which facilitated the mass-loss and electrochemical test simultaneously. LI et al [138] also developed an erosion-corrosion test with static sample under the impact of high-velocity jet with different impact angles, as shown in Figs. 30(b, c), and a lot of work has been carried out by means of this test [139−141]. For instance, YI et al [139] pointed out that critical flow velocity of jet, which varied with the type of material and was affected by pitting corrosion induced by Cl^-, was one of the valid parameters to evaluate the erosion-corrosion resistance of passive metal materials. The corrosion and erosion-corrosion performances of a novel type of Fe-based amorphous metallic coatings (AMCs) prepared by activated combustion high-velocity air fuel spray (AC-HVAF) were studied by them, compared with those of HVAF AMC as well as 316L SS, as shown in Fig. 31 [140]. It was indicated from Fig. 31 that the erosion- corrosion rate of all three metallic materials under the pure erosion of distilled water was the highest one among the three performance list in the horizontal axis in Fig. 31. Synergies including corrosion-induced erosion and erosion-induced corrosion played a critical role in the process of erosion-corrosion in NaCl solution containing sand particles. Coincidentally, a similar testing system, as shown in Fig. 32, which was capable of emitting single particle with a defined velocity to impact the surface of sample at a fixed angle under the potentiostatic control was designed by SUN et al [142]. Moreover, HUANG et al [143] developed a comprehensive phenomenological model for erosion of material in slurry pipeline flow, which was in good agreement with the experimental results.

5.2 Tribocorrosion

In general, tribocorrosion is the chemical−mechanical process causing the degradation of a

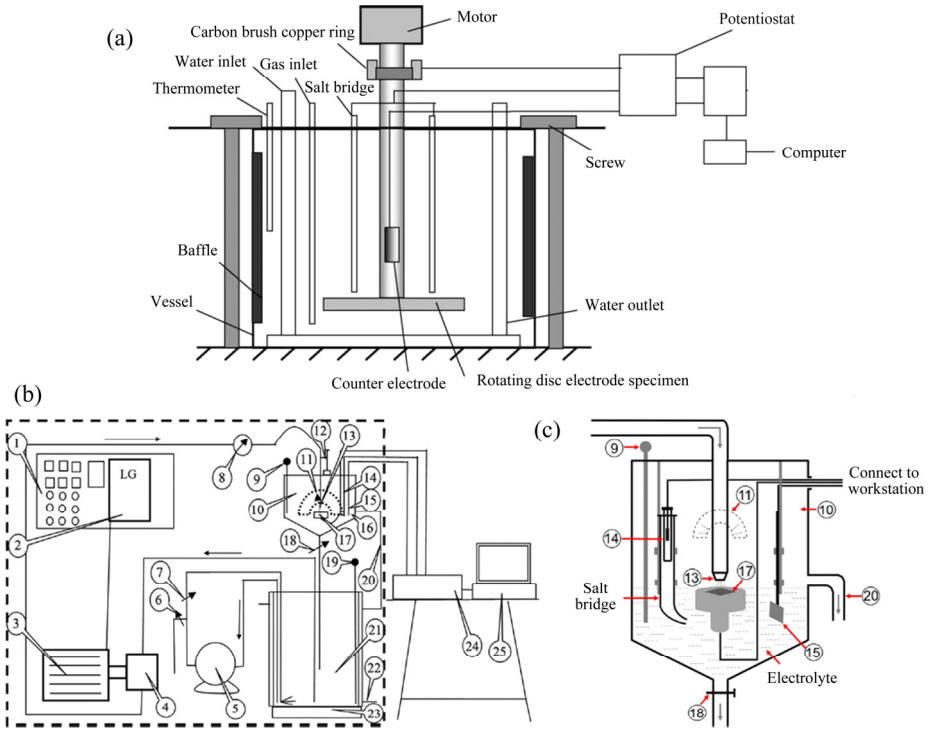

Fig. 30 Erosion-corrosion test designed by ZHENG et al [137,138]: (a) Modified erosion-corrosion test with rotating disc electrode specimens; (b, c) Erosion-corrosion test with static sample under impact of high-velocity jet with different impact angles

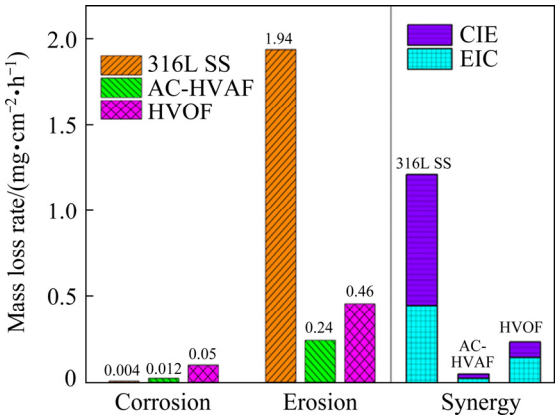

Fig. 31 Comparison of corrosion, erosion and synergy of AMC and 316L SS in tested solutions [140]

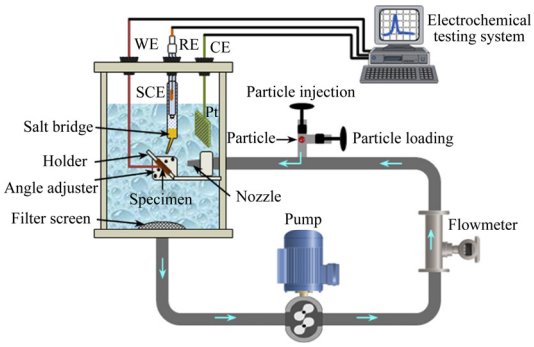

Fig. 32 Schematic diagram of apparatus for single particle impingement test and electrochemical measurement [142]

material exposed to an aggressive environment with a tribological contact. To some extent, the damage of materials caused by tribocorrosion is much more serious than that caused by erosion-corrosion in NaCl solution, which poses great challenge to reliability and durability of structural materials. Currently, a large number of efforts have been made to investigate the tribocorrosion or corrosive-wear behaviors of coating materials under combined electrochemical and mechanical actions in NaCl solution [144−149]. According to the configuration of the friction pair, the tribocorrosion test can also be divided into two types: block-on-ring and pin/ball-on-disk.

To further improve the tribocorrosion resistance of metal substrate, PLSs (i.e., TiSiCN/Ag, CrN/CrCN, and Cr/graphite-like carbon (GLC)) were deposited on the substrate [144,145]. According to the experimental results carried out by pin-on-disk reciprocation tribometer equipped with a three-electrode electrochemical workstation, as shown in Fig. 33(a) [144], PLSs coating

significantly enhanced the tribocorrosion resistance of metal substrate in artificial seawater due to the deflection of the propagation of crack, as shown in Fig. 33(b) [146]. Additionally, the tribocorrosion performance of PLS could be enhanced by thickening the top-layer and optimizing the multilayer structure [144], which could also prolong the diffusion path of corrosive species.

Another type of tribocorrosion test is performed by a block-on-ring configuration, as shown in Fig. 34 [147]. By using this test, LEE et al [147] reported that Ni−P coating exhibited high tribocorrosion performance in NaCl solution and the synergy effect between corrosion and wear dominated the degradation of coating.

6 Corrosion in deep-sea

Currently, deep-sea resource (i.e., oil, gas and minerals) exploitation is increasing. With the exception of Cl^- induced corrosion, the corrosion and corrosion-wear in deep-sea environment are

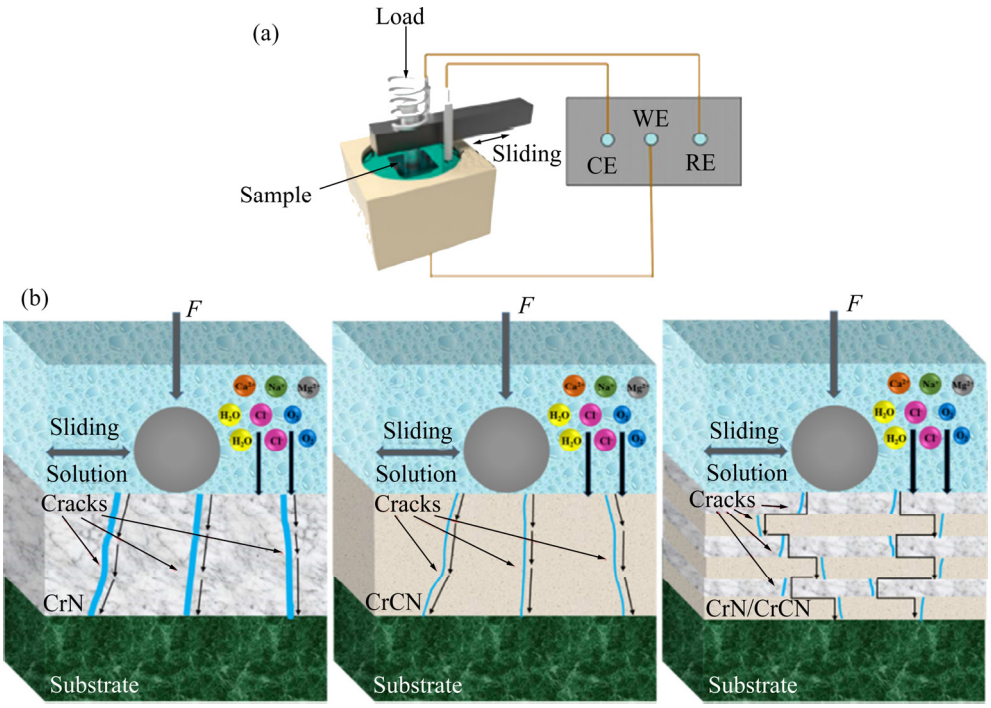

Fig. 33 Schematic diagram of tribocorrosion setup (a) [144], and improvement mechanism of tribocorrosion resistance of CrN/CrCN PLSs coating (b) [146]

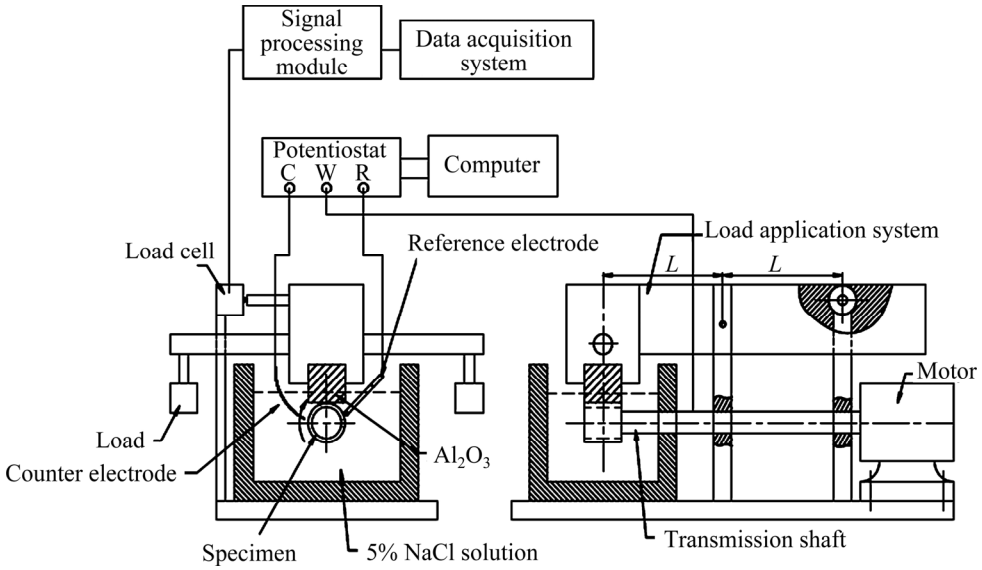

Fig. 34 Schematic diagram for setup of block-on-dist tribocorrosion tester [147]

characterized by less sunlight, high hydrostatic, high salinity, a low dissolved oxygen content and a low water temperature. Studies on corrosion and corrosion-wear in deep-sea environment have to face formidable challenges. The deep-sea corrosion experiments are of great cost and high technically demand [150−153].

A type of deep-sea corrosion experimental setup with deployment and retrieval using mooring line technology was developed by TRAVERSO and CANEPA [150] as shown in Fig. 35. It was proved that hydrostatic pressure promoted the anodic dissolution and suppressed self-healing of passive protective film in deep-sea. While, controversy on the role of the adsorption and penetration of Cl^- on the corrosion in deep-sea still exists. WANG et al [153] found that hydrostatic pressure could increase the adsorption and penetration of Cl^-, and promote the proliferation of point defects in oxides passive film, leading to the rapid pitting corrosion. While, LIU et al [154] found that the adsorption of Cl^- at the corrosion front did not play an important role in the enhancement of corrosion process caused by hydrostatic pressure. On the contrary, a thin Helmholtz layer was the main reason for the promoted anodic dissolution.

The tribocorrosion resistance of Ti6Al4V alloy under the simulated deep-sea environment was studied by using a high pressure tribo-electrochemical apparatus as shown in Fig. 36(a) [152], which was under the pin-on-disk structure and permitted tribocorrosion test and in-situ electrochemical measurement. It was found that the tribocorrosion of Ti alloy differed from atmospheric pressure to

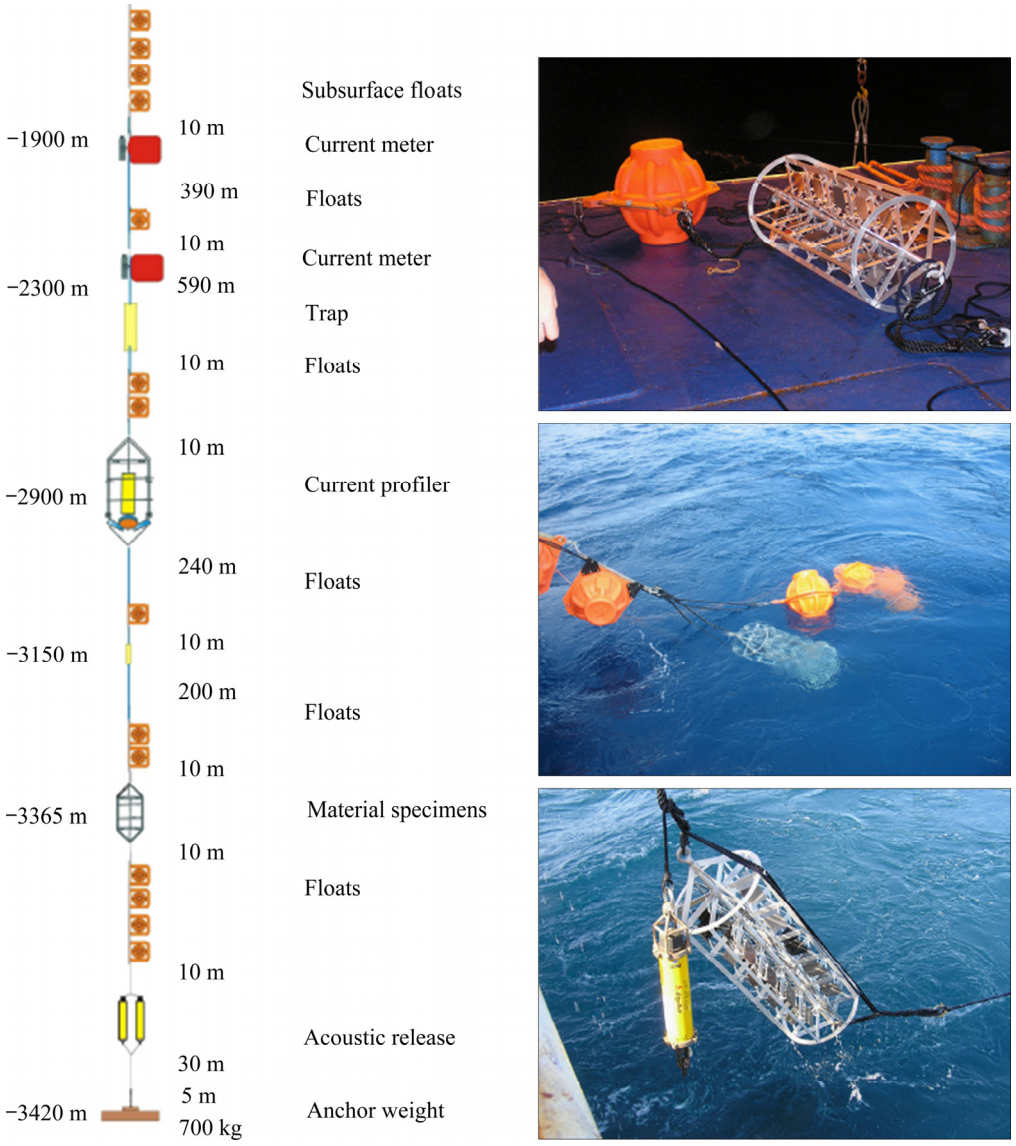

Fig. 35 Experimental setup for deep-sea corrosion experiment [150]

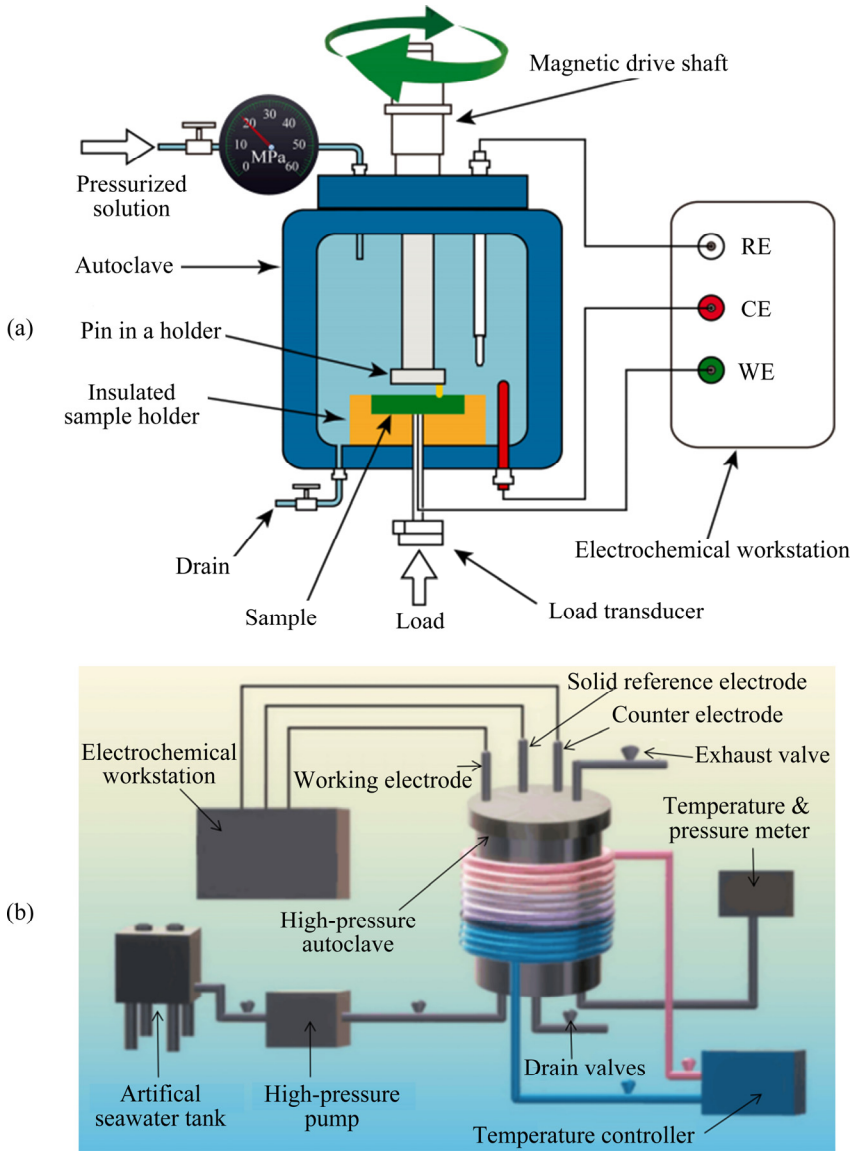

Fig. 36 Schematic illustration of high pressure tribo-electrochemical apparatus (a) [152], and deep-sea simulation device (b) [155]

hydrostatic pressure and the degradation was dominated by delaminated wear as the hydrostatic pressure increased to a critical value due to the convergence of micro-cracks and corrosion pits [152]. Wear accelerated by corrosion was the main failure mechanism under a high hydrostatic pressure. The corrosion behavior and growth defect evolution of Cr/GLC PLS in artificial seawater was studied by the device as shown in Fig. 36(b) [155]. It was proved that the galvanic corrosion between the Cr and GLC layers combined with the shearing force induced by the high hydrostatic pressure would destroy the structure of the penetrating defects introduced during the deposition process. Meanwhile, the high hydrostatic pressure promoted the diffusion process of corrosive media through the penetrating defects and accelerated the exposure of the substrate. Thus, it is an eternal issue to improve the interfacial structure between the coating and substrate.

In a word, materials suffered from serious damage caused by corrosion-wear, especial the synergy between electrochemical corrosion and mechanical degradation. Corrosion speeds up wear and vice-versa. In addition to experimental results provided by types of corrosion-wear testers, numerical simulation based on FE or other models has also been developed to predict the corrosion-wear behaviours of metallic materials in NaCl solution, which would provide a guideline for

future material design and optimization against corrosion-wear in aggressive environment [156−158].

7 Other degradation induced by Cl^- corrosion

Because of a thinner effective cross-section or thickness of material and the surface defects (i.e., pit, void and crack) introduced by corrosion and the interaction between corrosion and mechanical load, many secondary damages, like HE, stress corrosion cracking (SCC), corrosion fatigue (CF) and cavitation erosion may happen and lead to the degradation of materials eventually.

Strictly speaking, HE is the phenomenon that metal materials degrade at a lower level of load due to the deterioration of mechanical properties caused by dissolved hydrogen atoms [29]. As mentioned above, hydrogen is created during the process of corrosion reaction especially in Cl^--containing environment, so it can diffuse into the corroded bulk metal. HE is one of the most critical corrosion failures in oil and gas industry as well as in construction [159]. Compared with other types of steels, the austenitic SS is the most resistant to HE. Attempts have made to improve the HE resistance and create a consensus that the HE resistance is primarily regulated by the PLSs regardless of types of bulk metals because of their hydrogen-trapping effects [28,160]. In addition, surface treatment techniques can also hinder H entry behavior. It was suggested that hot-dipped Al−Mg−Si sacrificial coating was favourable for high-strength steel applications with smaller risk of HE, compared with that of the conventional zinc galvanised coating [161]. These coatings could act as H permeation barrier. Recently, molecular simulations and atomistic simulations have been developed to understand the H transport and HE mechanism. Although the simulation results were in agreement with experimental date, more advanced simulations and targeted experiments were needed to deeply validate the proposed mechanism of HE [29].

ALMUAILI et al [162] observed the reactivation of a corrosion pit under the synergetic effect of unidirectional tensile strain and electrochemical polarisation in NaCl solution by using SR-μCT. Visual appearance of a new pit after the reactivation was shown. Pit growth kinetics increased dramatically due to the strain-induced reactivation. Corrosion fatigue is caused by the simultaneous effect of corrosive environment and alternating loads, which has become the common failure model especially for cable wires of long-span cross-sea bridges [163].

8 Conclusions and outlook

Corrosion, in particular, pitting corrosion caused in Cl^--containing environment, is very serious, which inevitably restricts the lifespan of materials. Although it is an old issue in the fields of material science and engineering, increasing efforts have been made to study the corrosion behaviors of materials, including traditional materials like DSSs, which have a high potential for ocean engineering applications, and novel materials like HEAs, with both fabricated by traditional manufacturing method or AM respectively, in the past decade. Herein, we reviewed recent progresses in understanding the degradation mechanism and improving the corrosion resistance and corrosion-wear resistance of materials ranging from bulk metal to surface treatment involving organic coating, metal and its alloy or compound coating. Hot-dipped Al−Zn alloy coating can provide effective cathodic protection in Cl^--containing environment, partially attributed to the important role of layered double hydroxide, which is also highlighted. It is greatly noted that, among the progresses in improving anti-corrosion property, the PLSs outperform others, wherever in terms of bulk metal or surface treatment, regardless of aggressive environment (corrosion or corrosion- wear conditions), which paves the way for more advanced anti-corrosion design. In addition, advanced characterization methods with multi-scale and high spatial resolution and two/three-dimensional numerical simulation based on kinds of models at different scales were developed to help deeply understand the process of corrosion and/or corrosion-wear in the Cl^--containing aqueous environment. Combined experimental result with numerical simulation, the micro-galvanic corrosion dominated degradation mechanism of PLSs was critically analyzed. Meanwhile, types of setups to realize corrosion-wear in laboratory were summarized. At last, corrosion-induced degradation like HE and CF was also simply introduced. However, due to the multidisciplinary characteristic

of anti-corrosion design, limited by the author's knowledge, it is hard to fully explore all the corresponding research simultaneously. We hope that this review article will arise more attention on the harms of corrosion and spur more deep theory and engineering research on the corrosion protection methodology.

For future lines of research, in order to improve the corrosion resistance in Cl^--containing aqueous environment, there are still important challenges as follows: (1) The effect of grain size on the corrosion performance is controversial, attempts are greatly needed to elucidate the essential relationship between grain size and corrosion resistance from the view of mechanism and balance the competition between dissolution effect of grain boundary and barrier/passivation effect of increased interfaces from the technical perspective, respectively. (2) It is urgent to further optimize the parameters of AM to eliminate microstructural defects like porosity, inclusions and residual stress and to form a most favorable CLM. (3) It is very necessary to combine high-accuracy experimental data obtained by means of multi-scale (macro, micro-meso, and nano-atomic) characterization with advanced simulation method, further optimize the compositions of the layers and the width between mutually parallel laminae in PLS and deeply study its degradation mechanism coupled with other coatings or phases on atomic scale. Similarly, inspired by this, the corresponding research including pitting corrosion initiation and propagation on the PLS consisting of more than two alternating layers like LPSO phase, with each layer aiming for specific functionalities, initiates a new direction in the field of anti-corrosion. (4) A variety of corrosion-wear tests lead to that quantitative anti-corrosion property is hard to be unified, thus, standard experimental equipment and methods are greatly urgent to satisfy the demand of anti-corrosion in the marine engineering.

Acknowledgments

The authors are grateful for the financial supports from the National Natural Science Foundation of China (Nos. 42066003, 51701053), Hainan Provincial Natural Science Foundation of China (Nos. 420RC522, 517076), and the Shanghai Synchrotron Radiation Facility, China (Nos. 2018-SSRF-PT-003860, A01202001004).

References

[1] LI X G, ZHANG D W, LIU Z Y, LI Z, DU C W, DONG C F. Materials science: Share corrosion data [J]. Nature, 2015, 527(7579): 441−442.

[2] BU Y Y, AO J P. A review on photoelectrochemical cathodic protection semiconductor thin films for metals [J]. Green Energy & Environment, 2017, 2(4): 331−362.

[3] ZHANG X M, CHEN W P. Review on corrosion-wear resistance performance of materials in molten aluminum and its alloys [J]. Transactions of Nonferrous Metals Society of China, 2015, 25(6): 1715−1731.

[4] KOUSHIK B G, van der STEEN N, MAMME M H, van INGELGEM Y, TERRYN H. Review on modelling of corrosion under droplet electrolyte for predicting atmospheric corrosion rate [J]. Journal of Materials Science & Technology, 2021, 62: 254−267.

[5] XHANARI K, FINŠGAR M. Organic corrosion inhibitors for aluminum and its alloys in chloride and alkaline solutions: A review [J]. Arabian Journal of Chemistry, 2019, 12(8): 4646−4663.

[6] SOLTIS J. Passivity and passivity breakdown [M]// Encyclopedia of Interfacial Chemistry. Amsterdam: Elsevier, 2018: 396−400.

[7] HOU B R, LI X G, MA X M, DU C W, ZHANG D W, ZHENG M, XU W C, LU D Z, MA F B. The cost of corrosion in China [J]. Npj Materials Degradation, 2017, 1: 4.

[8] GROCHOLSKI B. Tracking corroding chloride [J]. Science, 2018, 361(6406): 989.

[9] WANG Y K. Ultimate strength and mechano-electrochemical investigations of steel marine structures subject to corrosion [D]. Southampton: University of Southampton, 2015.

[10] WANG Y K, WHARTON J A, SHENOI R A. Ultimate strength analysis of aged steel-plated structures exposed to marine corrosion damage: A review [J]. Corrosion Science, 2014, 86: 42−60.

[11] HOU Bao-rong, ZHANG Dun, WANG Peng. Marine corrosion and protection: Current status and prospect [J]. Bulletin of Chinese Academy of Sciences, 2016, 31(12): 1326−1331. (in Chinese)

[12] VERMA C, EBENSO E E, QURAISHI M A. Corrosion inhibitors for ferrous and non-ferrous metals and alloys in ionic sodium chloride solutions: A review [J]. Journal of Molecular Liquids, 2017, 248: 927−942.

[13] MARCIALES A, PERALTA Y, HAILE T, CROSBY T, WOLODKO J. Mechanistic microbiologically influenced corrosion modeling: A review [J]. Corrosion Science, 2019, 146: 99−111.

[14] YI Y, ZHU D J, GUO S C, ZHANG Z H, SHI C J. A review on the deterioration and approaches to enhance the durability of concrete in the marine environment [J]. Cement and Concrete Composites, 2020, 113: 103695.

[15] ALMUAILI F A. Characterisation of 3D pitting corrosion kinetics of stainless steel in chloride containing environments [D]. Manchester: University of Manchester, 2017.

[16] BHANDARI J, KHAN F, ABBASSI R, GARANIYA V, OJEDA R. Modelling of pitting corrosion in marine and offshore steel structures—A technical review [J]. Journal of Loss Prevention in the Process Industries, 2015, 37: 39−62.

[17] ZHANG B, WANG J, WU B, GUO X W, WANG Y J, CHEN D, ZHANG Y C, DU K, OGUZIE E E, MA X L. Unmasking chloride attack on the passive film of metals [J]. Nature Communications, 2018, 9: 2559.

[18] LOTO R T. Effect of SO_4^{2-} and Cl^- anionic attack on the localized corrosion resistance and morphology of 409 ferritic stainless steel [J]. Results in Physics, 2019, 12: 738−742.

[19] ZHANG B, MA X L. A review—Pitting corrosion initiation investigated by TEM [J]. Journal of Materials Science & Technology, 2019, 35(7): 1455−1465.

[20] XIE Y, ZHANG J S, ALDEMIR T, DENNING R. Multi-state Markov modeling of pitting corrosion in stainless steel exposed to chloride-containing environment [J]. Reliability Engineering and System Safety, 2018, 172: 239−248.

[21] SOLTIS J. Passivity breakdown, pit initiation and propagation of pits in metallic materials — Review [J]. Corrosion Science, 2015, 90: 5−22.

[22] XIE Y, GUO S Q, LEONG A, ZHANG J S, ZHU Y K. Corrosion behaviour of stainless steel exposed to highly concentrated chloride solutions [J]. Corrosion Engineering, Science and Technology, 2017, 52(4): 283−293.

[23] AHMAD Z. Principles of corrosion engineering and corrosion control [M]. 1st ed. Burlington: Elsevier, 2006.

[24] DJUKIC M B, BAKIC G M, ZERAVCIC V S, SEDMAK A, RAJICIC B. The synergistic action and interplay of hydrogen embrittlement mechanisms in steels and iron: Localized plasticity and decohesion [J]. Engineering Fracture Mechanics, 2019, 216: 106528.

[25] YIN S Q, DUAN W C, LIU W H, WU L, YU J M, ZHAO Z L, LIU M, WANG P, CUI J Z, ZHANG Z Q. Influence of specific second phases on corrosion behaviors of Mg−Zn−Gd−Zr alloys [J]. Corrosion Science, 2020, 166: 108419.

[26] RAJA V S, PADEKAR B S. Role of chlorides on pitting and hydrogen embrittlement of Mg−Mn wrought alloy [J]. Corrosion Science, 2013, 75: 176−183.

[27] HAN J, NAM J H, LEE Y K. The mechanism of hydrogen embrittlement in intercritically annealed medium Mn TRIP steel [J]. Acta Materialia, 2016, 113: 1−10.

[28] SUN J J, JIANG T, SUN Y, WANG Y J, LIU Y N. A lamellar structured ultrafine grain ferrite-martensite dual-phase steel and its resistance to hydrogen embrittlement [J]. Journal of Alloys and Compounds, 2017, 698: 390−399.

[29] TEHRANCHI A, CURTIN W A. The role of atomistic simulations in probing hydrogen effects on plasticity and embrittlement in metals [J]. Engineering Fracture Mechanics, 2019, 216: 106502.

[30] CHENG L, YANG B S, WU Y J, ZHANG X, LIU J, ZHANG G H, WU K M. Experimental and numerical analysis of hydrogen diffusion behaviors in an ultra-fine bainitic steel [J]. International Journal of Hydrogen Energy, 2020, 45(46): 25493−25508.

[31] RYAN M P, WILLIAMS D E, CHATER R J, HUTTON B M, MCPHAIL D S. Why stainless steel corrodes [J]. Nature, 2002, 415(6873): 770−774.

[32] CWALINA K L, DEMAREST C R, GERARD A Y, SCULLY J R. Revisiting the effects of molybdenum and tungsten alloying on corrosion behavior of nickel-chromium alloys in aqueous corrosion [J]. Current Opinion in Solid State and Materials Science, 2019, 23(3): 129−141.

[33] ARTHANARI S, JANG J C, SHIN K S. Corrosion performance of high pressure die-cast Al−6Si−3Ni and Al−6Si−3Ni−2Cu alloys in aqueous NaCl solution [J]. Transactions of Nonferrous Metals Society of China, 2018, 28(11): 2181−2189.

[34] SNIHIROVA D, HÖCHE D, LAMAKA S, MIR Z, HACK T, ZHELUDKEVICH M L. Galvanic corrosion of Ti6Al4V -AA2024 joints in aircraft environment: Modelling and experimental validation [J]. Corrosion Science, 2019, 157: 70−78.

[35] ZENG Q F, XU Y T. A comparative study on the tribocorrosion behaviors of AlFeCrNiMo high entropy alloy coatings and 304 stainless steel [J]. Materials Today Communications, 2020, 24: 101261.

[36] CHEN Ming-dong, ZHANG Fan, LIU Zhi-yong, YANG Chao-hui, DING Guo-qing, LI Xiao-gang. Galvanic series of metals and effect of alloy compositions on corrosion resistance in Sanya seawater [J]. Acta Metallurgica Sinca, 2018, 54(9): 1311−1321. (in Chinese)

[37] SOUFEIANI L, FOLIENTE G, NGUYEN K T Q, SAN NICOLAS R S. Corrosion protection of steel elements in facade systems: A review [J]. Journal of Building Engineering , 2020, 82: 101759.

[38] SHI Y Z, YANG B, LIAW P K. Corrosion-resistant high-entropy alloys: A review [J]. Metals, 2017, 7(2): 43.

[39] ZHU J Y, LI D P, CHANG W, WANG Z, HU L H, ZHANG Y N, WANG M M, YANG Z W, SONG J W, CHEN S L, ZHANG L, ZHANG L. In situ marine exposure study on corrosion behaviors of five alloys in coastal waters of western Pacific Ocean [J]. Journal of Materials Research and Technology, 2020, 9(4): 8104−8116.

[40] KADOWAKI M, MUTO I, SUGAWARA Y, DOI T, KAWANO K, HARA N. Pitting corrosion resistance of martensite of AISI 1045 steel and the beneficial role of interstitial carbon [J]. Journal of the Electrochemical Society, 2017, 164(14): C962−C972.

[41] IANNUZZI M, BARNOUSH A, JOHNSEN R. Materials and corrosion trends in offshore and subsea oil and gas production [J]. Npj Materials Degradation, 2017, 1: 2.

[42] ZHANG B, WEI X X, WU B, WANG J, SHAO X H, YANG L X, ZHENG S J, ZHOU Y T, JIN Q Q, OGUZIE E E, MA X L. Chloride attack on the passive film of duplex alloy [J]. Corrosion Science, 2019, 154: 123−128.

[43] CHENG X Q, WANG Y, DONG C F, LI X G. The beneficial galvanic effect of the constituent phases in 2205 duplex stainless steel on the passive films formed in a 3.5% NaCl solution [J]. Corrosion Science, 2018, 134: 122−130.

[44] RALSTON K D, BIRBILIS N, DAVIES C H J. Revealing the relationship between grain size and corrosion rate of metals [J]. Scripta Materialia, 2010, 63(12): 1201−1204.

[45] CHENG X Q, WANG Y, LI X G, DONG C F. Interaction between austein-ferrite phases on passive performance of 2205 duplex stainless steel [J]. Journal of Materials Science & Technology, 2018, 34(11): 2140−2148.

[46] WANG P J, MA L W, CHENG X Q, LI X G. Effect of grain size and crystallographic orientation on the corrosion behaviors of low alloy steel [J]. Journal of Alloys and Compounds, 2021, 857: 158258.

[47] FU X Q, JI Y C, CHENG X Q, DONG C F, FAN Y, LI X G. Effect of grain size and its uniformity on corrosion resistance of rolled 316L stainless steel by EBSD and TEM [J]. Materials Today Communications, 2020, 25: 101429.

[48] LUO Y F, DENG Y L, GUAN L Q, YE L Y, GUO X B, LUO A. Effect of grain size and crystal orientation on the corrosion behavior of as-extruded Mg−6Gd−2Y−0.2Zr alloy [J]. Corrosion Science, 2020, 164: 108338.

[49] TANG J W, CHEN L, LI Z G, ZHAO G Q, ZHANG C S. Formation of abnormal coarse grains and its effects on corrosion behaviors of solution treated ZK60 Mg alloy [J]. Corrosion Science, 2021, 180: 109201.

[50] CHEN Y F, YANG B, ZHOU Y T, WU Y, ZHU H H. Evaluation of pitting corrosion in duplex stainless steel Fe20Cr9Ni for nuclear power application [J]. Acta Materialia, 2020, 197: 172−183.

[51] RALSTON K D, BIRBILIS N. Effect of grain size on corrosion: A review [J]. Corrosion, 2010, 66(7): 75005.

[52] LIU C, LI X, REVILLA R I, SUN T, ZHAO J B, ZHANG D W, YANG S F, LIU Z Y, CHENG X Q, TERRYN H, LI X G. Towards a better understanding of localised corrosion induced by typical non-metallic inclusions in low-alloy steels [J]. Corrosion Science, 2021, 179: 109150.

[53] ZHENG S J, WANG Y J, ZHANG B, ZHU Y L, LIU C, HU P, MA X L. Identification of $MnCr_2O_4$ nano-octahedron in catalysing pitting corrosion of austenitic stainless steels [J]. Acta Materialia, 2010, 58(15): 5070−5085.

[54] ZHOU Y T, ZHANG B, ZHENG S J, WANG J, SAN X Y, MA X L. Atomic-scale decoration for improving the pitting corrosion resistance of austenitic stainless steels [J]. Scientific Reports, 2014, 4: 3604.

[55] SAN X Y, ZHANG B, WU B, WEI X X, OGUZIE E E, MA X L. Investigating the effect of Cu-rich phase on the corrosion behavior of Super 304H austenitic stainless steel by TEM [J]. Corrosion Science, 2018, 130: 143−152.

[56] KNIGHT S P, BIRBILIS N, MUDDLE B C, TRUEMAN A R, LYNCH S P. Correlations between intergranular stress corrosion cracking, grain-boundary microchemistry, and grain-boundary electrochemistry for Al−Zn−Mg−Cu alloys [J]. Corrosion Science, 2010, 52(12): 4073−4080.

[57] SUN S H, ISHIMOTO T, HAGIHARA K, TSUTSUMI Y, HANAWA T, NAKANO T. Excellent mechanical and corrosion properties of austenitic stainless steel with a unique crystallographic lamellar microstructure via selective laser melting [J]. Scripta Materialia, 2019, 159: 89−93.

[58] HEMMASIAN ETTEFAGH A, GUO S M, RAUSH J. Corrosion performance of additively manufactured stainless steel parts: A review [J]. Additive Manufacturing, 2021, 37: 101689.

[59] LALEH M, HUGHES A E, YANG S, LI J L, XU W, GIBSON I, TAN M Y. Two and three-dimensional characterisation of localised corrosion affected by lack-of-fusion pores in 316L stainless steel produced by selective laser melting [J]. Corrosion Science, 2020, 165: 108394.

[60] SUHAILA S. Modelling pitting corrosion in carbon steel materials [D]. Manchester: University of Manchester, 2013.

[61] de MEO D, OTERKUS E. Finite element implementation of a peridynamic pitting corrosion damage model [J]. Ocean Engineering, 2017, 135: 76−83.

[62] GHAHARI S M, KROUSE D P, LAYCOCK N J, RAYMENT T, PADOVANI C, SUTER T, MOKSO R, MARONE F, STAMPANONI M, MONIR M, DAVENPORT A J. Pitting corrosion of stainless steel: Measuring and modelling pit propagation in support of damage prediction for radioactive waste containers [J]. Corrosion Engineering, Science and Technology, 2011, 46(2): 205−211.

[63] JAFARZADEH S, CHEN Z G, ZHAO J M, BOBARU F. Pitting, lacy covers, and pit merger in stainless steel: 3D peridynamic models [J]. Corrosion Science, 2019, 150: 17−31.

[64] CHEN Z G, ZHANG G F, BOBARU F. The influence of passive film damage on pitting corrosion [J]. Journal of the Electrochemical Society, 2015, 163(2): C19−C24.

[65] JAFARZADEH S, CHEN Z G, BOBARU F. Computational modeling of pitting corrosion [J]. Corrosion Reviews, 2019, 37(5): 419−439.

[66] ROKKAM S, GUNZBURGER M, BROTHERS M, PHAN N, GOEL K. A nonlocal peridynamics modeling approach for corrosion damage and crack propagation [J]. Theoretical and Applied Fracture Mechanics, 2019, 101: 373−387.

[67] CHADWICK A F, STEWART J A, ENRIQUE R A, DU S C, THORNTON K. Numerical modeling of localized corrosion using phase-field and smoothed boundary methods [J]. Journal of the Electrochemical Society, 2018, 165(10): C633−C646.

[68] LIN C, RUAN H H. Multi-phase-field modeling of localized corrosion involving galvanic pitting and mechano-electrochemical coupling [J]. Corrosion Science, 2020, 177: 108900.

[69] FATOBA O O, LEIVA-GARCIA R, LISHCHUK S V, LARROSA N O, AKID R. Simulation of stress-assisted localised corrosion using a cellular automaton finite element approach [J]. Corrosion Science, 2018, 137: 83−97.

[70] CUI C J, MA R J, CHEN A R, PAN Z C, TIAN H. Experimental study and 3D cellular automata simulation of corrosion pits on Q345 steel surface under salt-spray environment [J]. Corrosion Science, 2019, 154: 80−89.

[71] WU S C, XIAO T Q, WITHERS P J. The imaging of failure in structural materials by synchrotron radiation X-ray microtomography [J]. Engineering Fracture Mechanics, 2017, 182: 127−156.

[72] ALMUAILI F A, MCDONALD S A, WITHERS P J, ENGELBERG D L. Application of a quasi in situ experimental approach to estimate 3-D pitting corrosion kinetics in stainless steel [J]. Journal of the Electrochemical Society, 2016, 163(13): C745−C751.

[73] WEI L, LIU Y, LI Q, CHENG Y F. Effect of roughness on general corrosion and pitting of $(FeCoCrNi)_{0.89}(WC)_{0.11}$ high-entropy alloy composite in 3.5 wt.% NaCl solution [J]. Corrosion Science, 2019, 146: 44−57.

[74] XU Z L, ZHANG H, DU X J, HE Y Z, LUO H, SONG G S, MAO L, ZHOU T W, WANG L L. Corrosion resistance enhancement of CoCrFeMnNi high-entropy alloy fabricated by additive manufacturing [J]. Corrosion Science, 2020, 177:

108954.

[75] ZHU Y K, FREE M L, WOOLLAM R, DURNIE W. A review of surfactants as corrosion inhibitors and associated modeling [J]. Progress in Materials Science, 2017, 90: 159−223.

[76] SHARMA S, KUMAR A. Recent advances in metallic corrosion inhibition: A review [J]. Journal of Molecular Liquids, 2021, 322: 114862.

[77] MONTEMOR M F. Functional and smart coatings for corrosion protection: A review of recent advances [J]. Surface & Coatings Technology, 2014, 258: 17−37.

[78] DING R, CHEN S, LV J, ZHANG W, ZHAO X D, LIU J, WANG X, GUI T J, LI B J, TANG Y Z, LI W H. Study on graphene modified organic anti-corrosion coatings: A comprehensive review [J]. Journal of Alloys and Compounds, 2019, 806: 611−635.

[79] WEI J, WEI Y H, LI J, ZHAO H T, LV C X, DONG J H, KE W, HE X Y. Corrosion behavior of damaged epoxy coated steel bars under the coupling effect of chloride ion and carbonization [J]. Acta Metallurgica Sinica, 2020, 56(6): 885−897.

[80] JIANG Q, MIAO Q, LIANG W P, YING F, TONG F, XU Y, REN B L, YAO Z J, ZHANG P Z. Corrosion behavior of arc sprayed Al−Zn−Si−RE coatings on mild steel in 3.5 wt.% NaCl solution [J]. Electrochimica Acta, 2014, 115: 644−656.

[81] LEE H S, SINGH J K, PARK J H. Pore blocking characteristics of corrosion products formed on aluminum coating produced by arc thermal metal spray process in 3.5 wt.% NaCl solution [J]. Construction and Building Materials, 2016, 113: 905−916.

[82] BORGIOLI F, GALVANETTO E, BACCI T. Corrosion behaviour of low temperature nitrided nickel-free, AISI 200 and AISI 300 series austenitic stainless steels in NaCl solution [J]. Corrosion Science, 2018, 136: 352−365.

[83] KAYALI Y, ANATURK B. Investigation of electrochemical corrosion behavior in a 3.5 wt.% NaCl solution of boronized dual-phase steel [J]. Materials & Design, 2013, 46: 776−783.

[84] GAO Z Q, ZHANG D W, QIU X P, JIANG S M, WU Y C, ZHANG Q F, LI X G. The mechanisms of corrosion inhibition of hot-dip galvanized steel by vanadyl oxalate: A galvanic corrosion investigation supported by XPS [J]. Corrosion Science, 2018, 142: 153−160.

[85] CHANG J K, LIN C S, WANG W R. Oxidation and corrosion behavior of commercial 5 wt.% Al−Zn coated steel during austenitization heat treatment [J]. Surface and Coatings Technology, 2018, 350: 880−889.

[86] DUCHOSLAV J, STEINBERGER R, ARNDT M, KEPPERT T, LUCKENEDER G, STELLNBERGER K H, HAGLER J, ANGELI G, RIENER C K, STIFTER D. Evolution of the surface chemistry of hot dip galvanized Zn−Mg−Al and Zn coatings on steel during short term exposure to sodium chloride containing environments [J]. Corrosion Science, 2015, 91: 311−320.

[87] SUN K L, YAN S, YU T P, WANG K H, FENG C, XU L K, XIE G W. Highly enhanced photoelectrochemical cathodic protection performance of the preparation of magnesium oxides modified TiO_2 nanotube arrays [J]. Journal of Electroanalytical Chemistry, 2019, 834: 138−144.

[88] LIU Q, MA R N, DU A, ZHANG X R, YANG H Z, FAN Y Z, ZHAO X, CAO X M. Investigation of the anticorrosion properties of graphene oxide doped thin organic anticorrosion films for hot-dip galvanized steel [J]. Applied Surface Science, 2019, 480: 646−654.

[89] SHARMA V, SHARMA V, GOYAT M S, HOODA A, PANDEY J K, KUMAR A, GUPTA R, UPADHYAY A K, PRAKASH R, KIRABIRA J B, MANDAL P, BHARGAV P K. Recent progress in nano-oxides and CNTs based corrosion resistant superhydrophobic coatings: A critical review [J]. Progress in Organic Coatings, 2020, 140: 105512.

[90] VAZIRINASAB E, JAFARI R, MOMEN G. Application of superhydrophobic coatings as a corrosion barrier: A review [J]. Surface and Coatings Technology, 2018, 341: 40−56.

[91] ZHANG F, JU P F, PAN M Q, ZHANG D W, HUANG Y, LI G L, LI X G. Self-healing mechanisms in smart protective coatings: A review [J]. Corrosion Science, 2018, 144: 74−88.

[92] LI S W, GAO B, TU G F, HU L, SUN S C, ZHU G L, YIN S H. Effects of magnesium on the microstructure and corrosion resistance of Zn−55Al−1.6Si coating [J]. Construction and Building Materials, 2014, 71: 124−131.

[93] YAO C Z, LV H B, ZHU T P, ZHENG W G, YUAN X D, GAO W. Effect of Mg content on microstructure and corrosion behavior of hot dipped Zn−Al−Mg coatings [J]. Journal of Alloys and Compounds, 2016, 670: 239−248.

[94] LIU W, LI M C, LUO Q, FAN H Q, ZHANG J Y, LU H S, CHOU K C, WANG X L, LI Q. Influence of alloyed magnesium on the microstructure and long-term corrosion behavior of hot-dip Al−Zn−Si coating in NaCl solution [J]. Corrosion Science, 2016, 104: 217−226.

[95] LIU W, LI Q, LI M C. Corrosion behaviour of hot-dip Al−Zn−Si and Al−Zn−Si−3Mg coatings in NaCl solution [J]. Corrosion Science, 2017, 121: 72−83.

[96] LI S W, GAO B, YIN S H, TU G F, ZHU G L, SUN S C, ZHU X P. The effects of RE and Si on the microstructure and corrosion resistance of Zn−6Al−3Mg hot dip coating [J]. Applied Surface Science, 2015, 357: 2004−2012.

[97] PROSEK T, NAZAROV A, GOODWIN F, ŠERÁK J, THIERRY D. Improving corrosion stability of ZnAlMg by alloying for protection of car bodies [J]. Surface and Coatings Technology, 2016, 306: 439−447.

[98] LI Y. Formation of nano-crystalline corrosion products on Zn−Al alloy coating exposed to seawater [J]. Corrosion Science, 2001, 43(9): 1793−1800.

[99] BUKHTIYAROVA M V. A review on effect of synthesis conditions on the formation of layered double hydroxides [J]. Journal of Solid State Chemistry, 2019, 269: 494−506.

[100] ZHANG G, WU L, TANG A T, MA Y L, SONG G L, ZHENG D J, JIANG B, ATRENS A, PAN F S. Active corrosion protection by a smart coating based on a MgAl-layered double hydroxide on a cerium-modified plasma electrolytic oxidation coating on Mg alloy AZ31 [J]. Corrosion Science, 2018, 139: 370−382.

[101] SONG Y H, TANG Y, FANG L, WU F, ZENG X G, HU J, ZHANG S F, JIANG B, LUO H J. Enhancement of corrosion resistance of AZ31 Mg alloys by one-step in situ synthesis of ZnAl-LDH films intercalated with organic anions (ASP, La) [J]. Journal of Magnesium and Alloys, 2021, 9(2): 658−667.

[102] VOLOVITCH P, VU T N, ALLÉLY C, AAL A A, OGLE K. Understanding corrosion via corrosion product

characterization: II. Role of alloying elements in improving the corrosion resistance of Zn−Al−Mg coatings on steel [J]. Corrosion Science, 2011, 53(8): 2437−2445.

[103] ZHANG X M, CHEN W P, LUO H F, LI S, ZHOU T. Effects of Cr and Zn on the interfacial microstructures of borides in Fe−Cr−B cast steels during hot-dipping in Al−Zn alloys [J]. International Journal of Materials Research, 2019, 110(3): 202−208.

[104] ZHANG X, LEYGRAF C, ODNEVALL WALLINDER I. Atmospheric corrosion of Galfan coatings on steel in chloride-rich environments [J]. Corrosion Science, 2013, 73: 62−71.

[105] VU A Q, VUILLEMIN B, OLTRA R, ALLÉLY C. Cut-edge corrosion of a Zn−55Al-coated steel: A comparison between sulphate and chloride solutions [J]. Corrosion Science, 2011, 53(9): 3016−3025.

[106] ZAMANZADE M, BARNOUSH A. Effect of chromium on the electrochemical properties of iron aluminide intermetallics [J]. Corrosion Science, 2014, 78: 223−232.

[107] BYUN J M, BANG S R, KIM H W, KIM T Y, HONG S J, KIM Y D. Effect of heat treatment on corrosion resistance and adhesion property in Zn−Mg−Zn multi-layer coated steel prepared by PVD process [J]. Surface and Coatings Technology, 2017, 309: 1010−1014.

[108] WANG W, WANG D, HAN F S. Improvement of corrosion resistance of twinning-induced plasticity steel by hot-dipping aluminum with subsequent thermal diffusion treatment [J]. Materials Letters, 2019, 248: 60−64.

[109] SHI Z M, CAO J B, HAN F S. Preparation and characterization of Fe−Al intermetallic layer on the surface of T91 heat-resistant steel [J]. Journal of Nuclear Materials, 2014, 447(1−3): 77−81.

[110] DANZO I I, HOUBAERT Y, VERBEKEN K. Diffusion driven columnar grain growth induced in an Al−Si-coated steel substrate [J]. Surface and Coatings Technology, 2014, 251: 15−20.

[111] CUBIDES Y, KARAYAN A I, ZHAO D X, NASH L, XIE K, CASTANEDA H. New insights on the corrosion mechanism of a peak-aged Mg−9Al−1Zn alloy in a chloride environment [J]. Journal of Alloys and Compounds, 2020, 840: 155786.

[112] ZHAO Y C, ZHAO M C, XU R, LIU L, TAO J X, GAO C D, SHUAI C J, ATRENS A. Formation and characteristic corrosion behavior of alternately lamellar arranged α and β in as-cast AZ91 Mg alloy [J]. Journal of Alloys and Compounds, 2019, 770: 549−558.

[113] ZHAO M C, LIU M, SONG G L, ATRENS A. Influence of the β-phase morphology on the corrosion of the Mg alloy AZ91 [J]. Corrosion Science, 2008, 50(7): 1939−1953.

[114] NIE Y J, DAI J W, LI X, ZHANG X B. Recent developments on corrosion behaviors of Mg alloys with stacking fault or long period stacking ordered structures [J]. Journal of Magnesium and Alloys, 2021, 9(4): 1123−1146.

[115] WANG L S, JIANG J H, LIU H, SALEH B, MA A B. Microstructure characterization and corrosion behavior of Mg−Y−Zn alloys with different long period stacking ordered structures [J]. Journal of Magnesium and Alloys, 2020, 8(4): 1208−1220.

[116] XU D K, HAN E H, XU Y B. Effect of long-period stacking ordered phase on microstructure, mechanical property and corrosion resistance of Mg alloys: A review [J]. Progress in Natural Science: Materials International, 2016, 26(2): 117−128.

[117] SRINIVASAN A, BLAWERT C, HUANG Y, MENDIS C L, KAINER K U, HORT N. Corrosion behavior of Mg−Gd−Zn based alloys in aqueous NaCl solution [J]. Journal of Magnesium and Alloys, 2014, 2(3): 245−256.

[118] FEI J Y, WILCOX G D. Electrodeposition of zinc-nickel compositionally modulated multilayer coatings and their corrosion behaviours [J]. Surface and Coatings Technology, 2006, 200(11): 3533−3539.

[119] RASHMI S, ELIAS L, CHITHARANJAN HEGDE A. Multilayered Zn−Ni alloy coatings for better corrosion protection of mild steel [J]. Engineering Science and Technology, an International Journal, 2017, 20(3): 1227−1232.

[120] LEI Z F, ZHANG Q Q, ZHU X D, MA D X, MA F, SONG Z X, FU Y Q. Corrosion performance of ZrN/ZrO_2 multilayer coatings deposited on 304 stainless steel using multi-arc ion plating [J]. Applied Surface Science, 2018, 431: 170−176.

[121] BAHADORMANESH B, GHORBANI M. Ni−P/Zn−Ni compositionally modulated multilayer coatings — Part 2: Corrosion and protection mechanisms [J]. Applied Surface Science, 2018, 442: 313−321.

[122] LI G, ZHANG L, CAI F, YANG Y, WANG Q M, ZHANG S H. Characterization and corrosion behaviors of TiN/TiAlN multilayer coatings by ion source enhanced hybrid arc ion plating [J]. Surface and Coatings Technology, 2019, 366: 355−365.

[123] LIU J H, CHEN J L, LIU Z, YU M, LI S M. Fabrication of Zn−Ni/Ni−P compositionally modulated multilayer coatings [J]. Materials and Corrosion, 2013, 64(4): 335−340.

[124] LELEVIC A, WALSH F C. Electrodeposition of NiP alloy coatings: A review [J]. Surface and Coatings Technology, 2019, 369: 198−220.

[125] CROSS S R, WOOLLAM R, SHADEMAN S, SCHUH C A. Computational design and optimization of multilayered and functionally graded corrosion coatings [J]. Corrosion Science, 2013, 77: 297−307.

[126] CHEN Z G, BOBARU F. Peridynamic modeling of pitting corrosion damage [J]. Journal of the Mechanics and Physics of Solids, 2015, 78: 352−381.

[127] ZHANG X M, LUO H F, SHI L Y. Periodic layered structure formed during the interfacial reaction: A Review [J]. Journal of Iron and Steel Research, International, 2016, 23(11): 1127−1133.

[128] CHEN Yong-chong, LU Qi. The analysis of periodic layer formation during solid state reactions [J]. Acta Metallurgica Sinica, 2005, 41(3): 235−241. (in Chinese)

[129] ZHANG X M, CHEN W P, LUO H F, LING Z C, WANG J, ZHOU T, LI S. Influence of Cr on the interfacial boride reaction between Fe−Cr−B cast steel and molten aluminium [J]. Corrosion Science, 2019, 158: 108098.

[130] THIJS L, MONTERO SISTIAGA M L, WAUTHLE R, XIE Q G, KRUTH J P, van HUMBEECK J V. Strong morphological and crystallographic texture and resulting yield strength anisotropy in selective laser melted tantalum [J]. Acta Materialia, 2013, 61(12): 4657−4668.

[131] NGO T D, KASHANI A, IMBALZANO G, NGUYEN K T Q, HUI D. Additive manufacturing (3D printing): A review of materials, methods, applications and challenges [J] Composites Part B: Engineering, 2018, 143: 172−196.

[132] LU X C, LI S Z, JIANG X X, ZHANG T C. Effect of γ phase on corrosive wear of duplex stainless steel in sulfuric acid solution [J]. Corrosion, 1995, 51(6): 456−462.

[133] ARIBO S, BARKER R, HU X M, NEVILLE A. Erosion-corrosion behaviour of lean duplex stainless steels in 3.5% NaCl solution [J]. Wear, 2013, 302(1/2): 1602−1608.

[134] TIAN J, HUANG H L, PAN Z Q, ZHOU H. Effect of flow velocity on corrosion behavior of AZ91D magnesium alloy at elbow of loop system [J]. Transactions of Nonferrous Metals Society of China, 2016, 26(11): 2857−2867.

[135] ZHANG G A, ZENG L, HUANG H L, GUO X P. A study of flow accelerated corrosion at elbow of carbon steel pipeline by array electrode and computational fluid dynamics simulation [J]. Corrosion Science, 2013, 77: 334−341.

[136] ZENG L, ZHANG G A, GUO X P, CHAI C W. Inhibition effect of thioureidoimidazoline inhibitor for the flow accelerated corrosion of an elbow [J]. Corrosion Science, 2015, 90: 202−215.

[137] JIANG X, ZHENG Y G, KE W. Effect of flow velocity and entrained sand on inhibition performances of two inhibitors for CO_2 corrosion of N80 steel in 3% NaCl solution [J]. Corrosion Science, 2005, 47(11): 2636−2658.

[138] LI L L, WANG Z B, ZHENG Y G. Interaction between pitting corrosion and critical flow velocity for erosion-corrosion of 304 stainless steel under jet slurry impingement [J]. Corrosion Science, 2019, 158: 108084.

[139] YI J Z, HU H X, WANG Z B, ZHENG Y G. Comparison of critical flow velocity for erosion-corrosion of six stainless steels in 3.5 wt.% NaCl solution containing 2 wt.% silica sand particles [J]. Wear, 2018, 416/417: 62−71.

[140] WANG Y, XING Z Z, LUO Q, RAHMAN A, JIAO J, QU S J, ZHENG Y G, SHEN J. Corrosion and erosion-corrosion behaviour of activated combustion high-velocity air fuel sprayed Fe-based amorphous coatings in chloride-containing solutions [J]. Corrosion Science, 2015, 98: 339−353.

[141] ZHENG Z B, ZHENG Y G, SUN W H, WANG J Q. Effect of applied potential on passivation and erosion-corrosion of a Fe-based amorphous metallic coating under slurry impingement [J]. Corrosion Science, 2014, 82: 115−124.

[142] SUN C, LI J K, FATTAHPOUR V, ROOSTAEI M, MAHMOUDI M, ZENG H B, LUO J L. Insights into the erosion-enhanced corrosion on electroless Ni−P coating from single particle impingement [J]. Corrosion Science, 2020, 166: 108422.

[143] HUANG C K, MINEV P, LUO J L, NANDAKUMAR K. A phenomenological model for erosion of material in a horizontal slurry pipeline flow [J]. Wear, 2010, 269(3/4): 190−196.

[144] LI L, LIU L L, LI X W, GUO P, KE P L, WANG A Y. Enhanced tribocorrosion performance of Cr/GLC multilayered films for marine protective application [J]. ACS Applied Materials & Interfaces, 2018, 10(15): 13187−13198.

[145] DONG M P, ZHU Y B, XU L F, REN X R, MA F L, MAO F X, LI J L, WANG L P. Tribocorrosion performance of nano-layered coating in artificial seawater [J]. Applied Surface Science, 2019, 487: 647−654.

[146] WANG Y X, ZHANG J W, ZHOU S G, WANG Y C, WANG C T, WANG Y X, SUI Y F, LAN J B, XUE Q J. Improvement in the tribocorrosion performance of CrCN coating by multilayered design for marine protective application [J]. Applied Surface Science, 2020, 528: 147061.

[147] LEE H B, WUU D S, LEE C Y, LIN C S. Wear and immersion corrosion of Ni−P electrodeposit in NaCl solution [J]. Tribology International, 2010, 43(1/2): 235−244.

[148] FU Y Q, ZHOU F, WANG Q Z, ZHANG M D, ZHOU Z F. Electrochemical and tribocorrosion performances of CrMoSiCN coating on Ti−6Al−4V titanium alloy in artificial seawater [J]. Corrosion Science, 2020, 165: 108385.

[149] FU Y Q, ZHOU F, ZHANG M D, WANG Q Z, ZHOU Z F. Structural, mechanical and tribocorrosion performances of CrMoSiN coatings with various Mo contents in artificial seawater [J]. Applied Surface Science, 2020, 525: 146629.

[150] TRAVERSO P, CANEPA E. A review of studies on corrosion of metals and alloys in deep-sea environment [J]. Ocean Engineering, 2014, 87: 10−15.

[151] CANEPA E, STIFANESE R, MEROTTO L, TRAVERSO P. Corrosion behaviour of aluminium alloys in deep-sea environment: A review and the KM3NeT test results [J]. Marine Structures, 2018, 59: 271−284.

[152] REN P W, MENG H M, XIA Q J, ZHU Z Z, HE M T. Influence of seawater depth and electrode potential on the tribocorrosion of Ti6Al4V alloy under the simulated deep-sea environment by in-situ electrochemical technique [J]. Corrosion Science, 2021, 180: 109185.

[153] WANG X H, FAN L, DING K K, XU L K, GUO W M, HOU J, DUAN T G. Pitting corrosion of 2Cr13 stainless steel in deep-sea environment [J]. Journal of Materials Science & Technology, 2021, 64: 187−194.

[154] LIU R, CUI Y, LIU L, WANG F H. Study on the mechanism of hydrostatic pressure promoting electrochemical corrosion of pure iron in 3.5% NaCl solution [J]. Acta Materialia, 2021, 203: 116467.

[155] LIU Y R, DU H, ZUO X, GUO P, LIU L, LEE K R, WANG A Y, KE P L. Cr/GLC multilayered coating in simulated deep-sea environment: Corrosion behavior and growth defect evolution [J]. Corrosion Science, 2021, 188: 109528.

[156] WANG K W, WANG Y N, YUE X W, CAI W J. Multiphysics modeling and uncertainty quantification of tribocorrosion in aluminum alloys [J]. Corrosion Science, 2021, 178: 109095.

[157] NAZIR M H, KHAN Z A, SAEED A, SIDDAIAH A, MENEZES P L. Synergistic wear-corrosion analysis and modelling of nanocomposite coatings [J]. Tribology International, 2018, 121: 30−44.

[158] FALLAHNEZHAD K, OSKOUEI R H, TAYLOR M. Development of a fretting corrosion model for metallic interfaces using adaptive finite element analysis [J]. Finite Elements in Analysis and Design, 2018, 148: 38−47.

[159] HUANG C S, GAO X S. Phase field modeling of hydrogen embrittlement [J]. International Journal of Hydrogen Energy, 2020, 45(38): 20053−20068.

[160] YU S H, LEE S M, LEE S, NAM J H, LEE J S, BAE C M, LEE Y K. Effects of lamellar structure on tensile properties

and resistance to hydrogen embrittlement of pearlitic steel [J]. Acta Materialia, 2019, 172: 92−101.
[161] KYO Y, YADAV A P, NISHIKATA A, TSURU T. Hydrogen entry behaviour of hot-dip Al−Mg−Si coated steel [J]. Corrosion Science, 2011, 53(11): 3866−3871.
[162] ALMUAILI F A, MCDONALD S A, WITHERS P J, COOK A B, ENGELBERG D L. Strain-induced reactivation of corrosion pits in austenitic stainless steel [J]. Corrosion Science, 2017, 125: 12−19.
[163] XUE S L, SHEN R L, CHEN W, SHEN L L. The corrosion-fatigue measurement test of the Zn−Al alloy coated steel wire [J]. Structures, 2020, 27: 1195−1201.

金属材料在含氯化物水基环境中的耐腐蚀性能

张先满[1]，陈再雨[1]，罗洪峰[1]，周 腾[1]，赵愈亮[2]，凌自成[3]

1. 海南大学 机电工程学院，海口 570228；
2. 东莞理工学院 机械工程学院 中子散射工程技术中心，东莞 523808；
3. 华北水利水电大学 材料学院，郑州 450045

摘 要：腐蚀，特别是海洋环境中发生的点蚀，导致材料服役寿命锐减并造成巨大的经济损失甚至环境破坏和灾难事故。在过去的十年中，针对材料在含氯化物水基环境的腐蚀行为开展了大量的研究工作。在此，综述从金属整体材料到包括有机涂层、金属及其合金或化合物涂层在内的表面处理的失效机理以及提高材料耐腐蚀性能和耐腐蚀–磨损性能的最新研究进展。其中，重点阐述周期性层片结构(PLSs)，该组织无论是存在于金属整体材料或是表面涂层中，不管是在腐蚀或腐蚀–磨损过程中都展现出优越的抗腐蚀性能。基于不同尺寸、不同模型的数值仿真可加深对氯离子环境中的腐蚀或腐蚀–磨损过程的理解，并根据实验结果与数值仿真，着重分析 PLSs 以微电偶腐蚀占主导的腐蚀机理。总结各种腐蚀–磨损试验设备。展望未来的研究趋势，期待未来能够提供基于防腐蚀方法学设计的 PLS 的基本应用。

关键词：点蚀；氯离子；周期性层片结构；电偶腐蚀；失效机理

(Edited by Xiang-qun LI)